SCUOLA DI DOTTORATO
UNIVERSITÀ DEGLI STUDI DI MILANO-BICOCCA

Department of Material science

Ph.D. program: Materials science and nanotechnology Cycle: XXXIII

Development of an effective tumor-targeted contrast agent for magnetic resonance imaging based on Mn/H-ferritin nanocomplexes

Surname: Tullio

Name: Chiara

Registration number: 754000

Tutor: Prof. Miriam Colombo

Co-tutor: Prof. Davide Prosperi

Coordinator: Prof. Marco Bernasconi

ANNO ACCADEMICO / ACADEMIC YEAR 2019/2020

Table of content

List of abbreviations

ANOVA	analysis of variance
B_0	external magnetic field
Ca	calcium
CAs	contrast agents
c_{CA}	concentration of contrast agent
CT	x-ray computed tomography
DEAE	diethylaminoethanol
DLS	dynamic light scattering
DMEM	Dulbecco's modified eagle's medium
DPDP	dipyridoxyl diphosphate
DTPA	diethylenetriaminepentaacetic acid
EMA	european medicine agency
EMF	electromotive force
Epf	epifluorescence
EPR	enhanced permeability and retention
EpRE	genetically defined electrophile response elements
FBS	fetal bovine serum
FDA	food and drug administration
Fe	iron
Gd	gadolinium

HEPES	4-(2-hydroxyethyl)-1-piperazineethanesulfonic acid
HER2	human epithelial growth factor 2 receptor
HFn	H-ferritin
HFn-AF660	alexa fluor660 labeled-HFn
i.v.	intravenous
ICP-OES	inductively coupled plasma - optical emission spectrometry
IPTG	isopropyl β-D-1-tiogalactopiranoside
IRP	iron-regulatory proteins
K-MES	2-(N-morpholino)ethanesulfonic acid potassium salt
M	net magnetization vector
Mn	manganese
Mn@HFn-HT	manganese loaded H-Ferritin at 65 °C
Mn@HFn-RT	manganese loaded H-Ferritin at room temperature
MPS	mononuclear phagocytic system
MRI	magnetic resonance imaging
MTT	3-(4,5-dimethyl-2-thiazolyl)-2,5-diphenyl- 2H-tetrazolium bromide
MW	molecular weight
M_{XY}	transverse magnetization vector
M_z	longitudinal magnetization vector
NMR	nuclear magnetic resonance
NPs	nanoparticles
OD	optical density

PBS	phosphate buffered saline
PEG	polyethylene glycol
PET	positron emission tomography
PRE	before the treatment
R	relaxation rate
r	relaxivity
RPMI	Roswell park memorial institute
RF	radio-frequency
ROI	region of interest
ROS	reactive oxygen species
RT	room temperature
SD	standard deviation
SDS-PAGE	sodium dodecyl sulphate - polyacrylamide gel electrophoresis
SE	standard error
SPECT	single photon emission tomography
T_1	longitudinal relaxation time
T_2	transverse relaxation time
TEM	transmission electron microscopy
Tf	transferrin
TfR1	transferrin receptor
τ_M	mean water residence time
τ_R	molecular tumbling
ω_0	Larmor frequency

Abstract

Magnetic resonance imaging is one of the most sophisticated diagnostic tools in clinic. Contrast agents (CAs) may be exploited to afford much clearer images of detectable organs and to reduce the risk of misdiagnosis, due to the limited sensitivity of the technique. Actually, only a few gadolinium-based CAs are approved for clinical use. Nevertheless, concerns over their toxicity remain and their administration is approved only under strict control. In the present study it is reported the synthesis and validation of a novel manganese-based CA, Mn@HFn-RT. Manganese is an endogenous paramagnetic metal able to produce a positive contrast like gadolinium, however it is estimated to cause lower toxicity for human body. Manganese ions have been efficiently loaded inside the shell of a recombinant human protein called H-ferritin that is recognized by cells overexpressing TfR1, including the majority of cancer cell. Mn@HFn-RT was characterized, showing excellent colloidal stability, superior relaxivity and good safety profile. From *in vitro* experiments it was possible to confirm the ability of Mn@HFn-RT to efficiently target cancer cells and thus favor the detection of the tumor region in a breast cancer *in vivo* model with very low metal dosages and showing rapid clearance. Mn@HFn-RT looks a promising CA candidate to be developed for MRI.

1. Introduction

1.1 Nanomedicine

Nanomedicine is a new field of medicine, specialized in exploiting the knowledge and the tools of nanotechnology for the prevention and treatment of disease. Commonly, it is defined nano a material at its nanometric scale (1 - 100 nm). Working at molecular size scale, its peculiarity is the ability to integrate biology and technology, interacting efficiently with biomolecules using unique physiochemical properties. In fact, multiples characteristics, such as optical, magnetic and electron properties, were shown to exhibit marked differences compared with corresponding bulk materials when confined to a length scales of a few nanometers[1]. Nanomedicine has focused on a wide range of applications thus far, including biosensors, tissue engineering and drug delivery, where the main goal is the possibility to increase safety and biocompatibility of conventional medicines, improving specific drug targeting and pharmacokinetic properties[2,3,4]. The main tools explored are nanoparticles (NPs), 3D nanomaterials with at least one dimension in the range 1 - 100 nm.

1.1.1 Nanoparticles for clinic

Many NPs have entered clinical practice, and even more are being investigated in trials for a broad variety of indications. Currently, there are about 50 nanodrugs approved by Food and Drug Administration (FDA), despite the huge amount of reports published every year in this field[5]. Delay for translation to clinical practice is principally derived by biodistribution and safety considerations of developed nanotechnology. Optimizing biodistribution enhances successful outcomes. Firstly, depending on the purpose of each NP, it has to be chosen the most appropriate administration route to obtain an efficient distribution in the region of interest (i.e., oral, pulmonary, topical, transdermal, intravenous (i.v.), intramuscular and subcutaneous)[6]. Physical and chemical NPs features play an important role in achieving proper circulation time and a successive clearance of the nanocomposites. In particular, after entering in blood circulation, they have to face different hurdles, including disintegration by protein adsorption, opsonization-mediated removal by mononuclear phagocytic system (MPS), or filtration by organs. The last excretion route is size dependent, since NPs with a diameter below 5 - 10 nm can reach out to renal filtration, while liver easily eliminates NPs with a size between 20 - 100 nm. Larger NPs, which are not excreted by urine or bile to feces, are eventually eliminated by the MPS present also in lymph nodes and spleen (Figure 1)[7].

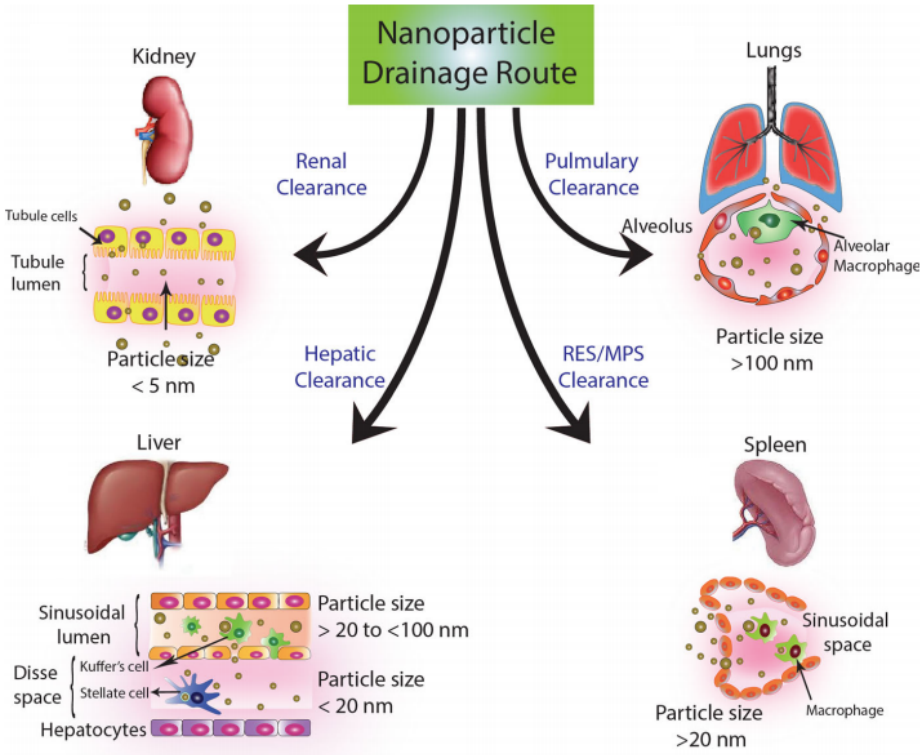

Figure 1. NPs drainage through different organs according to their properties. Reproduced with permission from the corresponding paper[7].

The occurrence of side effects is the other limiting step in clinical trials and can arise from multiple factors. Firstly, the material could provoke toxicity by itself or when administered in high concentrations (e.g., metal NPs). Moreover, NPs instability in the biological environment (where several proteins, molecules and pH changing are present) could induce aggregation and accumulation in tissues. Finally, inefficient clearance could also induce undesired NPs dissolution and production of reactive oxygen species (ROS)[8].

To overcome concerns about biodistribution and toxicity it is necessary to optimize NPs design, where factors impacting are resumed in Figure 2. In particular, size and shape play a crucial role in determining tissue penetration and cellular delivery: NPs with smaller size interact better with cell membrane and can result in a faster uptake[9]. Moreover, they are less recognized by macrophages provoking inferior inflammatory response[10]. Among multiple shapes, spherical NPs demonstrated to possess the faster internalization rate, followed by cubic, rods and disk-like NPs[11]. Also surface chemistry is a key factor in NPs synthesis: hydrophilic polymer coating is often required to stabilize NPs and to mask them from MPS (e.g., polyethylene glycol (PEG)). Surface charge can be tuned depending on the purposes, but generally NPs with a zeta potential higher than +30 mV or lower than -30 mV are considered stable[12].

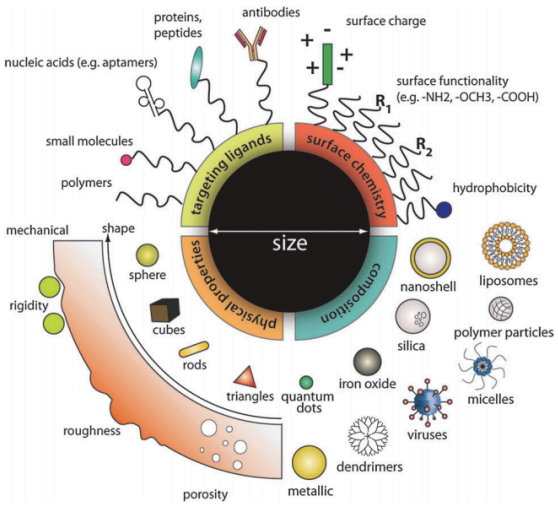

Figure 2. Tunable features to design NPs for clinical applications. Reproduced with permission from the corresponding paper[13].

1.1.2 Kinds of NPs

A wide range of materials have been exploited to produce NPs for different applications. Here, relevant for the purpose of the objective of this work, my discussion will focus on iron-, lipid- and protein- based NPs.

Iron-based NPs

Iron oxide NPs are a class of nanocomposites consisting of magnetite (Fe_3O_4) or maghemite (γ-Fe_2O_3), with a diameter variable between 1 and 100 nm. Among the different synthetic procedures, chemical preparations (e.g., coprecipitation, hydrothermal, microemulsion) are the most simple, efficient and cheap strategies[14,15]. The production of iron (Fe) NPs with a controlled size, composition and shape is achieved by modulating Fe(II) and Fe(III) ratio, pH and ionic. Using appropriate coating, iron oxide NPs can be converted into water soluble and bio-accessible nanocomposites, with a good biocompatibility and non-toxicity[16,17]. They can be exploited for several applications, such as drug delivery, and vaccine and antibody production[18,19,20]. Furthermore, the potential use in magnetic resonance imaging and hyperthermia treatments made them suitable as potential theranostic agents[21,22].

Lipid-based NPs

These nanovectors are generally composed by biomimetic and biodegradable materials and can be classified in two categories:

liposomes and solid lipid NPs. Liposomes are spherical vesicles composed by one or more phospholipidic bilayers and other biological constituents such as cholesterol and phosphatidylcholine, while lipid nanoparticles are composed by a solid liquid phase stabilized with a surfactant that promotes their solidity at body temperature[23]. Some advantages of the latter class include controlled release, targeting of active ingredients, increased stability and high payload[24]. Being the most advanced nonviral platforms approved in clinic to deliver small interfering RNA, many efforts are spent to synthetize new lipids capable to enhance selective targeting, long circulation or pH sensitivity[25,26]. Lipid-based NPs are highly used for therapeutic purposes and several formulations are actually available (e.g., Doxil®, Myocet®)[27,28,29].

Protein-based NPs

Biological structures have been exploited as potential nanovector. Their major advantages consist in their biodegradability and generally safe recognition from the immune system. Moreover, this kind of NPs may be obtained with simple preparative processes, higher drug payload and easier surface functionalization[30]. Albumin is a typical example of biological compound already approved for clinical purposes as excipient for vaccines or therapeutic protein drugs (e.g., Abraxane®)[31,32]. Other examples include self-assembled macromolecules such as ferritin, virus-like and vault cages[33,34,35].

1.1.3 Cancer in nanomedicine

1.1.3.1 Tumor targeting

NPs can reach selectively multiple kinds of cells, nevertheless cancer diagnosis and treatment are considered the field of election to date, thanks to the distinctive properties of the disease and the advantage achievable by small nanocomposites[36]. This pathology can affect different organs and tissues, provoking both uncontrolled cells division and acquisition of new structural and functional characteristics. This peculiarity was exploited by researchers to distinguish between healthy and malignant cells and favor an optimized targeting (Figure 3).

To direct NPs to tumor tissues the first strategy is passive targeting[37]. It was found that a growing tumor requires huge amounts of oxygen and nutrients, leading to an angiogenesis phenomenon. The blood vessels formed present defected architecture and various vascular permeability factors, facilitating transport of macromolecules larger than 40 kDa into malignant tissue[38]. Moreover, solid tumors are affected by weak lymphatic drainage, enhancing retention in those areas. The sum of the two factor is called EPR effect (enhanced permeability and retention)[39], and is considered a promising paradigm for anticancer drug and diagnosis development. Successful outcomes were already observed for several kinds of NPs, including micelle, liposomes, PLGA NPs and DNA polyplexes[40,41].

The functionalization of NPs with specific molecules allows to exploit also the active targeting. In fact, it was found that neoplastic cells overexpress particular proteins on their surface. For instance, human epithelial growth factor 2 receptor (HER2) was demonstrated to be upregulated in 15 - 30% of breast cancer and 10 - 15% of gastric/gastroesophageal cancers[42]. Another example is the transmembrane chondroitin sulfate proteoglycan 4, that was found to be overexpressed in 90% of primary and metastatic melanoma, but also in some leukemias and triple-negative breast carcinoma[43]. The interaction between receptors and targeting ligands linked on the surface of NPs (e.g., antibodies, peptides, aptamers) results in a specific and selective uptake by tumor cells, promoting an efficient targeting[44,45].

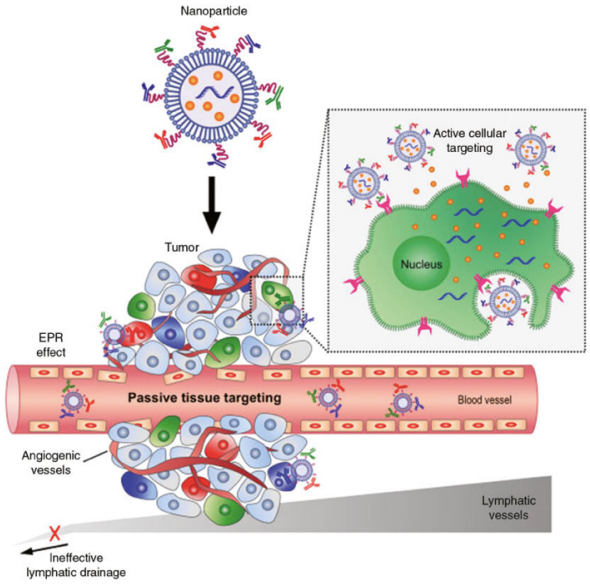

Figure 3. Passive and active targeting of NPs. Reproduced with permission from the corresponding paper[46].

1.1.3.2 Diagnosis in cancer

One of the most prominent field is diagnostic medicine, thanks to the significant benefits achievable by means of nanoscale size. Early diagnosis is the key to successfully treating many disorders, especially in oncological field. It is well know that solid tumors typically display Gompertzian kinetics, represented in Figure 4[47].

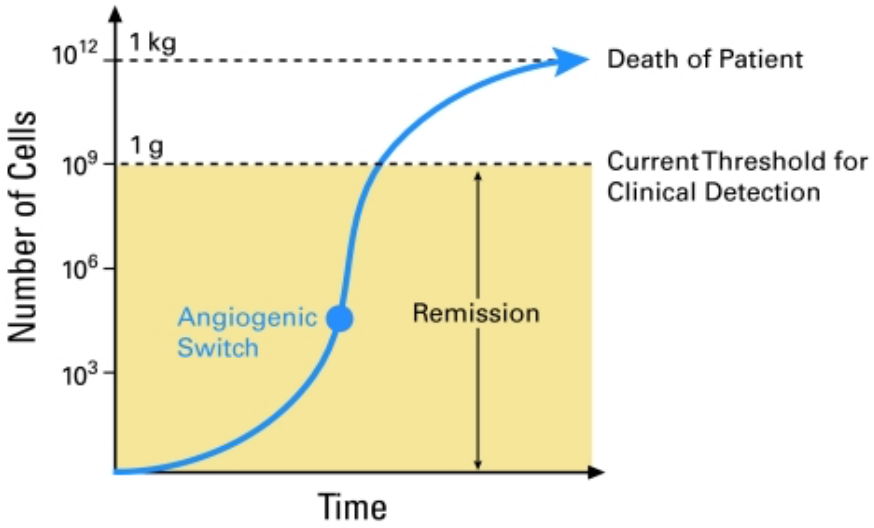

Figure 4. Gompertzian growth curve of a solid tumor and its relationship to cancer detection and imaging. Reproduced with permission from the corresponding paper[48].

Starting from a single cell, the number of malignant cells increases following an exponential but also slow trend. The trend continues until tumor mass reaches a dimension around 10^5 cells. At this stage, defined as angiogenic switch, different factors and modulators are produced to induce the formation of new blood vessels from a pre-existing

vasculature. Angiogenesis results in a higher amount of oxygen and nutrients nearby the cancer tissue and promotes its rapid proliferation. The process culminates, at worst, with the death of the patient at approximately 10^{12} cells (1 kg). Actually, the threshold to detect solid tumors is approximately 10^{9} cells (1 g = 1 cm^3). Reduce this limit is essential to diagnose the earlier stage of tumor formation, ideally before the angiogenic switch when the growth speed is still under control. This would increase the probability of therapy efficiency, furthermore it could also be useful to monitor the development of tumor mass. In fact, the first successful treatments are frequently capable to decrease its size below detection limit. However, it is hard to determine the eradication rate of malignant cells and to select the following drugs dosages. Therefore, the inefficiency or side effects derived from incorrect therapies would be limited reducing remission area.

Analytic tools with enhanced detection limit and sensitivity are required. In particular, four techniques are able to provide three-dimensional indication of tumor presence (Table 1[49]). Exploiting different approaches, each modality ensures a distinct performance in resolution, sensitivity and contrast generation, therefore the combination of multiple strategies enables the best results: x-ray computed tomography (CT) and magnetic resonance imaging (MRI) can furnish details on lesion location, size, morphology and structural changes to surrounding tissues; on the contrary, positron emission tomography (PET) and single photon emission tomography (SPECT) are ideal to investigate the tumor

physiology down to the molecular level, but don't provide anatomical details. Currently, many researchers are working to improve each of these techniques, trying to overcome the specific weakness. The technological advance is helping to speed up diagnostic improvements, although lots of work still need to be done.

Table 1. Methods used for molecular imaging in oncology. Reproduced with permission from the corresponding paper[49].

Method	Spatial Resolution	Temporal Resolution	Sensitivity [mol/L]	Costs	Advantages	Drawbacks
CT	50–200 μm	Minute	–	Low	Generation of anatomical images	It is difficult to generate functional, non-quantitative
MRI	25–100 μm	Minute to hour	10^{-3}–10^{-5}	Very high	High spatial resolution, non-radioactive tracers	Low sensitivity
PET	2–5 mm	Second to minute	10^{-11}–10^{-12}	Very high	The most sensitive imaging method, quantitative method, allows to use biologically relevant radionuclides	Imaging of large areas is expensive, low spatial resolution
SPECT	7.5–10 mm	Minute	10^{-10}–10^{-11}	High	Simultaneous multi-probe imaging is possible	Low spatial resolution

CT: Computed Tomography; MRI: Magnetic Resonance Imaging; PET: Positron Emission Tomography; SPECT: Single Photon Emission Computed Tomography.

1.2 Magnetic resonance imaging

Magnetic resonance imaging (MRI) has become one of the most suitable imaging technologies by means of its non-invasiveness, absence of radioactive substances and high spatial resolution performance. It exploits the principle of NMR, where the different energy produced by nuclear spin atoms under magnetic field is measurable. Generally, it is monitored the signal produced by the nucleus of hydrogen atom ^{1}H, since it is the most abundant isotopic form of magnetically active nuclei and possesses the highest gyromagnetic ratio[50]. To obtain a magnetic resonance image, the patient is placed inside a machine able to generate a static and uniform external magnetic field (B_0). As a result, each nuclear spin aligns along B_0 direction and starts to process with a specific frequency, known as Larmor frequency (ω_0) (Figure 5a). Net magnetization vector (M) is the sum of all spin magnetic moments generated[51] and it can be resolved into the two components: longitudinal (M_Z), that lies along B_0 direction, and transverse (M_{XY}), oriented along XY plane. Initially, M_Z is at its maximum (M_0), while M_{XY} is equal to zero. During the MRI scans, a series of resonance frequency pulse in the radio-frequency range (RF) is applied perpendicularly to B_0 (Figure 5b). Each RF leads to a simultaneous excitation of protons and a subsequent variation in M orientation, that aligns to RF direction. In this situation M_Z is zero, by contrast M_{XY} is at its maximum elongation[52].

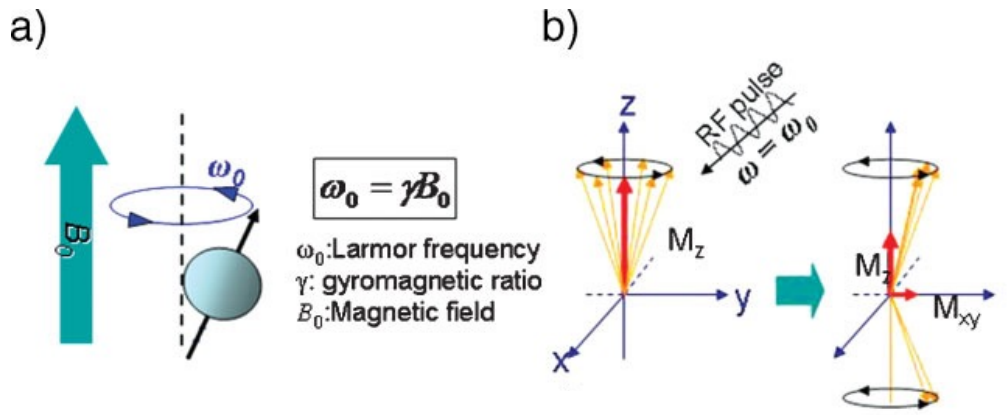

Figure 5. Principle of MRI. a) Spins align to the magnetic field and process under Larmor frequency (ω_0). b) After induction of RF pulse, magnetization of spins changes. The two components of M are visible. Modified and reproduced with permission from the corresponding paper[52].

When the applied RF is removed, the magnetic moment of the nuclei precesses in the static field. This last phenomenon is called relaxation, and the time it takes to be accomplished is defined relaxation time. It is measured in ms and it can be divided in two independent processes:

- T_1 longitudinal relaxation time: it is described by M_Z vector and it is also called the spin-lattice relaxation time because it refers to the time necessary for the spins to give the energy that they obtained from the RF pulse back to the surrounding lattice, in order to go back to their equilibrium state.
- T_2 transverse relaxation time: it is defined spin-spin relaxation, since it is the results of slightly differences in the magnetic environment created by the interaction between two adjacent proton spin. It refers to M_{XY} vector.

They can be obtained by two different equations, starting from the measurement of the evolution of M_Z or M_{XY} with time, as it is reported in Figure 6.

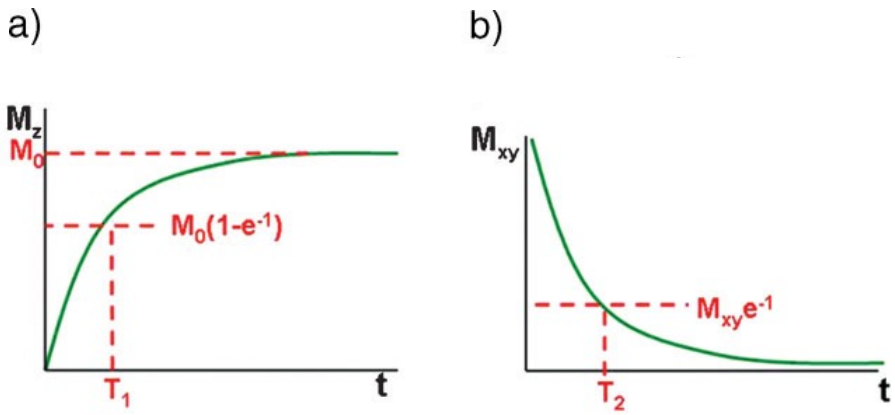

$$M_z\,(t) = M_0(1 - e^{-t/T_1})$$

$$M_{xy}\,(t) = M_0 e^{-t/T_2}$$

Figure 6. Graphical representation and relative equation of a) T_1 relaxation time and b) T_2 relaxation time. Modified and reproduced with permission from the corresponding paper[52].

In an MRI analysis it is possible to acquire relaxation times of specific portions of the body because the nuclear relaxation process produces energy, generating an electromotive force (EMF) measured by a receiver coil. This signal detected is elaborated to create an image. In particular, high EMF values are associated to brighter shade of gray, by contrast low values correspond to dark grey/black color[53].

Human tissues are considerably heterogeneous in terms of chemical and physical properties. Depending on the abundance of proteins and macromolecules there will be local perturbations of the magnetic field,

and a consequent dephasing in the precession process. The result is a T_2 relaxation time decrease. Moreover, the fluidity and the density of the environment play an important role in the energy transfer and modify the T_1 component (e.g. adipose tissues favor a shorter T_1 relaxation time)[53]. Every tissue lowers better one component, that is chosen to be investigated during an MRI exam since it will produce a stronger signal. The obtained images are examined by experts, and the presence of anomalous output can require further analysis.

1.2.1 Contrast agents

Diagnostic tool optimization could result in minimization of false positive or false negative outcomes as well as early disease detection. For this purpose, contrast agents (CAs) are often administered in patients and many efforts are spent to implement their efficacy. This is particularly important for MRI, since low sensitivity represents its main limitation. It is reported that 35% of MRI exams requires CAs administration[54], nevertheless huge concerns about their tolerability have resulted in a continuous investigation of new compounds.

A substance under a magnetic field can assume different behaviors, but only paramagnetic and superparamagnetic materials are able to increase a MR contrast. In fact, they can work as powerful microscopic local magnet, by modifying in particular the relaxation time of water protons present in the tissues. When they get close (i.e., ~ 0.1 - 1 nm), the protons are influenced by the large magnetic moment of the

paramagnetic/superparamagnetic ions and relax instantaneously, then rapidly exchange place with another unrelaxed water molecule, thus affecting the relaxation time[55]. This last effect is also called Proton relaxation enhancement[51].

Contrast enhancement is evaluated by the relaxation rate (R_i), where "i" refers to component 1 or 2. It is measured in s^{-1} and represents the inverse of relaxation time T_i. The capability of a CAs to respond efficiently to B_0 and to a RF impulse is defined relaxivity (r_i), and the value is calculated according to the following equation:

$$r_i = R_i / c_{CA}$$

where c_{CA} is the analytical concentration of the ion responsible of the contrast (unit of measure: $mM^{-1}\ s^{-1}$). It is dependent on the magnetic field applied and the temperature and results as higher as shorter the relaxation time[56].

Depending on their magnetic susceptibilities, CAs can be divided into T_1 positive or T_2 negative forms. T_1 CAs emphasize R_1, producing a positive contrast (brighter images), on the contrary T_2 CAs affect transverse component resulting in a negative contrast (darker images). r_2/r_1 ratio helps to discriminate between CAs suitable for positive or negative contrast: indeed, high values define T_2 CAs, while low values suggest the ability to produce hyperintense signal in T_1-wheighted images (Figure 7).

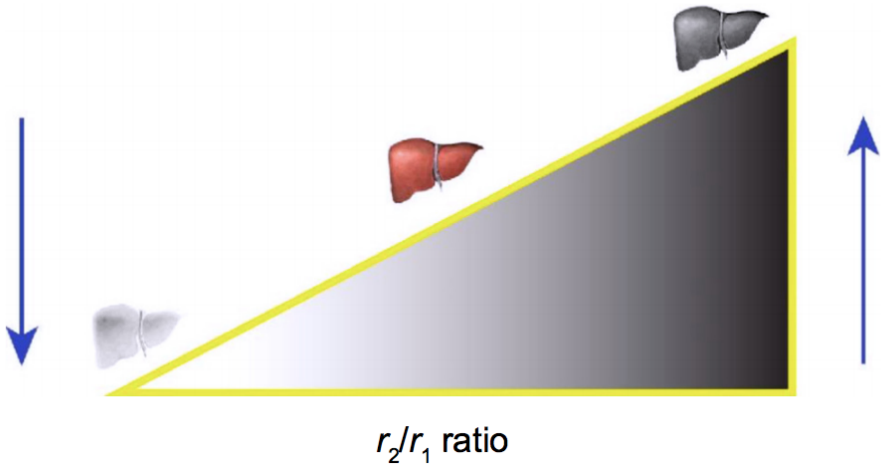

Figure 7. Influence of the r_2/r_1 ratio on the efficiency of a contrast agent. Reproduced with permission from the corresponding paper[56].

1.2.1.1 Features and properties of contrast agents

Good CAs must efficiently shorten T_1 or T_2 relaxation time in tissues at low dosages avoiding acute side effects. High relaxivity needs a fast exchange between water molecules with the surrounding environment. Metal – water interaction relaxes excited ions further increasing relaxivity (Figure 8). It can be divided into an inner sphere and an outer sphere term. The inner sphere describes the effect originating from the closest water molecule interacting directly with the metal of the CAs: on the coordination site over million water protons are relaxed every second, since each molecule remains linked to the ion the time strictly necessary to be relaxed (τ_M, mean water residence time). On the contrary, the outer sphere represents the impact of the interactions between the ion and closely diffusing water molecules without a direct chemical bond. Due to

the distance, the effect is less strong, nevertheless the abundance of molecules involved in the outer sphere ensure a final decisive contribution to the relaxation process. In some cases, water molecules weakly interacting with the ion might constitute a second hydration sphere, which can lead to a second sphere relaxivity term. For clinical agents, 60% of the relaxivity originates from inner sphere relaxation and 40% from outer sphere effects[57].

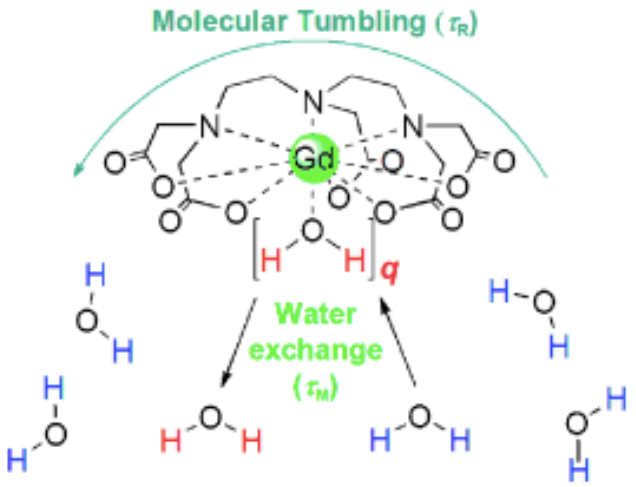

Figure 8. Selected factors that affect proton relaxivity. In blue and red are represented excited and relaxed water protons, respectively. Reproduced with permission from the corresponding paper[58].

A key factor that governs the efficiency of a CAs is the molecular tumbling (τ_R), relative to the rotational correlation time of the complex forming the CA itself. In particular, Solomon-Bloembergen-Morgan theory for paramagnetic relaxation predicts that increasing τ_R will enhance the

relaxivity of T_1 CAs. This occurs when the local magnetic field of the metal ion fluctuates at a frequency similar to Larmor frequency[59]. This strategy has been widely used to design biologically responsive agents. For example, τ_R can be made longer either by coupling the molecular motion of the agent to that of a larger structure such as binding to a protein[60] or by increasing the molecular size of the agent itself[61]. Both strategies slow tumbling of CAs and increase relaxivity.

Another important property is the tissue-specificity of a CA. The possibility to promote a specific biodistribution results in two important benefits: the accumulation of CAs in a defined site enhances the contrast efficiency in that region; in addition, it enables to lower the dosage with a consequent inferior toxicity. The dimension of the agents can be exploited to reach selectively some clearance organs (liver and kidney); otherwise the agents can be linked to specific molecules in order to target selected tissues (e.g., functionalized nano CAs for tumor detection).

Finally, a good CA should be characterized by a rapid clearance, because a fast excretion after the imaging test prevent metal ions accumulation in the tissues, followed by chronical toxicity. Clearance naturally occurs either by glomerular filtration or the hepatobiliary system.

1.2.1.2 Classification of contrast agents

There are many typologies of exogenous CAs: small mononuclear or polynuclear paramagnetic chelates, particulate CAs, metalloporphyrins,

polymeric or macromolecular carriers of covalently or noncovalently bonded paramagnetic chelates, and paramagnetic or superparamagnetic NPs. Among them, first CAs investigated belong to T_2 CAs category, like iron oxide NPs. Despite the high performance *in vitro*, several disadvantages limit the clinical applications. Gastromark™, Feridex I.V.® and Resovist® are example of superparamagnetic iron oxide particles commercialized in the past years, but discontinued from the market after manifestation of toxic effects and/or weak performances[62]. In fact, their administration produces images with lower contrast compared to T_1- weighted images. The risk of misdiagnosis is higher also because the dark signal can be confused with bleeding of tissues, calcification or metal deposition[52]. Moreover, the presence of T_2 CAs induces a distortion of the magnetic field on neighboring normal tissues. This artifact given by magnetic susceptibility is called “blooming effect” and demolishes the background around the lesions avoiding an efficient recognition of pathological conditions[63]. For all these reasons, positive CAs are preferred in clinic. Actually, they are mainly constituted by paramagnetic ions complexed with chelating groups.

1.2.1.2.1 Gadolinium

Lanthanides are a class of chemical elements that, in their trivalent ion form, possesses unpaired electron in 4f orbital and presents paramagnetic properties. Among them, the most powerful is gadolinium (Gd). Gd(III), thanks to its seven unpaired electrons, is the paramagnetic

ion that produce the highest magnetic moment. It is the most relevant lanthanide for clinic, nevertheless, it could be highly toxic in a biological system. Indeed, proteins are not able to distinguish between calcium (Ca) as Ca(II) and Gd(III), given the similar ionic radius and the higher positive charge. Consequently, a free Gd(III) ion can bind to Ca(II) channels[64] or Ca(II) requiring proteins such as calmodulin, calsequestrin, and calexitin, and can induce unrequested signals[65]. To avoid side effects, it is necessary to bound the ion with an organic linker or a chelating agent (linear or macrocyclic). The complex should be stable both in the period between the synthesis and the administration (shelf life) and inside the human body. A good clearance would minimize additional toxicity by secreting the complex before metal dissociation.

In 1987 Gd(III) complexed with diethylenetriaminepentaacetic acid (Gd-DTPA)[66] was approved for the detection of tumor brain formations with the commercial name Magnevist®. Many other compounds became available in clinic; however, several studies reported the insurgence of complications in patients affected by renal insufficiency. Their exposure to Gd caused thickening and darkening developing on large areas of the skin, provoking also pain and difficulty to move limbs. The pathology was named nephrogenic systemic fibrosis[67], and World Health Organization disallowed Gd-based CAs administration in people with hepatorenal syndrome. Later, new evidences described the deposition of Gd in central nervous system, bones, kidneys and other tissues in patients without severe renal disease[68]. For these reasons, in 2017 the European

Medicine Agency (EMA) confirmed recommendation to restrict the use of some linear Gd agents and to suspend the authorization of others[69]. The agents currently available in clinic are reported in Table 2.

Table 2. EMA's final decision on use of Gd agents in body scans.

Product	Type (formulation)	Recommendation
Artirem / Dotarem (gadoteric acid)	macrocyclic (i.v.)	maintain
Artirem / Dotarem (gadoteric acid)	macrocyclic (intra-articular)	maintain
Gadovist (gadobutrol)	macrocyclic (i.v.)	maintain
Magnevist (gadopentetic acid)	linear (intra-articular)	maintain
Magnevist (gadopentetic acid)	linear (i.v.)	suspend
Multihance (gadobenic acid)	linear (i.v.)	restrict to liver scans
Omniscan (gadodiamide)	linear (i.v.)	suspend
Optimark (gadoversetamide)	linear (i.v.)	suspend
Primovist (gadoxetic acid)	linear (i.v.)	maintain
Prohance (gadoteridol)	macrocyclic (i.v.)	maintain

A promising alternative for positive contrast in MRI is the utilization of a different paramagnetic ion: manganese (II).

1.2.1.2.2 Manganese

Manganese (Mn) is a transition metal found in nature in several minerals. It is a natural human cell constituent, necessary for lipid, carbohydrate, and protein metabolism. Different manganese metalloenzymes are involved in multiple organ functions, such as bone growth, normal immune function, digestion, regulation of blood glucose level and defense against free radicals[70]. In concert with vitamin K, Mn also supports blood coagulation. Given the wide range of applications, an adequate diet requires 2 – 10 mg of Mn/day[71].

Mn can exist in many oxidation state, among which Mn(II), (IV) and (VII) are the most important in biological compounds. Mn(II) ion possesses five unpaired electrons, that allows an efficient interaction with water molecules promoting their relaxation in a MR context. The paramagnetic effect is less pronounced compared with Gd, nevertheless the safer profile has led several research groups to develop new Mn-based CAs. They can be divided in two main categories: small molecule agents and nanoparticulate or macromolecular agents, depending on the organization of the metal.

a) Small molecule agents

Despite the powerful relaxivity, free Mn can't be administered in human body as $MnCl_2$ because it was found to promote neurotoxicity. Nevertheless, its usage is promoted for manganese-enhanced MRI contrast techniques developed in animals, with several applications, such as CAs for brain anatomical studies[72], marker of brain activity[73] and neuronal track tracer for several pathways[74]. Several molecules were investigated as potential chelating agents. Among them, an i.v. formulation of Mn chelated with dipyridoxyl diphosphate (Mn-DPDP; Teslascan®) was clinically available for more than a decade (Figure 9)[75]. However, it had to be administrated as a slow i.v. infusion over 15–20 min, which caused logistic difficulties and additional costs. It was withdrawn from the market in October 2003 in the U.S. and in July 2010 in Europe[76,77].

Another successful strategy exploited $MnCl_2$ encapsulation inside liposomes (LumenHance®)[78]: Bracco received marketing approval, nevertheless the product it is actually discontinued[79].

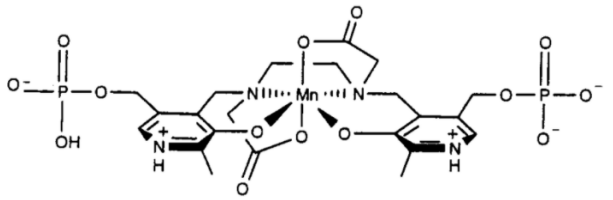

Figure 9. Molecular structure of Mn-DPDP. Reproduced with permission from the corresponding paper[80].

b) Nanoparticles and macromolecular agents

In the second approach, multiples Mn ions are packaged together to enhance the relaxivity properties. Mn-oxo clusters are a promising strategy, since chains of Mn, like the highly studied Mn-12 ($Mn_{12}O_{12}(O_2CCH_3)_{16}(H_2O)_4$) can rapidly exchange with water molecules. To improve their solubility and stability, they are normally attached to the surface of polymer beads[81]. Mn can also be incorporated to form effectively Mn-based NPs. The most investigated are Mn oxide NPs, whose surface is covered with different molecules or compounds (e.g., PEG, polyvinylpyrrolidone or silica) to endow hydrophilic properties and improve biocompatibility[82,83,84]. Although they are still in the early lab stage, NP CAs have demonstrated improved signal intensity, targeting ability and longer circulation time compared to conventional CAs, especially for cancer diagnosis. Indeed, exploiting both EPR effect and surface functionalization for active targeting, many studies reported efficient accumulations in tumor tissues [85,86,87]. Their limiting step can be attributed to technical assembly challenges, as well as issues regarding the Mn dose required for a successful contrast.

Actually, there are no clinical evidences of toxic effects of Mn-based CAs, nevertheless it has to be noticed that an overexposure to Mn (e.g., contaminated water and workers exposure) could provoke neurodegenerative disorders[88]. It is thus necessary to adopt specific precautions to minimize Mn accumulation in tissues.

1.3 Ferritin

Ferritin is a globular protein present in the majority of living species. It was discovered in 1937 by Victor Laufberg, who isolated the new protein from a horse spleen. Successive investigations concerning ferritin level in plasma showed its involvement in iron storage and bioavailability[89].

1.3.1 Structure

Ferritin is constituted of 24 subunits that self-assemble to form a spheric shell with octahedral symmetry of around 12 nm in diameter with an interior cavity of 8 nm (Figure 10)[90]. Twelve channels (0.3 - 0.4 diameter) are situated close to the junctions between subunits: among them, six are hydrophobic and suitable for proton transfer between inside the cavity and outside, whereas eight are hydrophilic and can be exploited for the passage of metal ions and small molecules[91]. It is well known that ferritin can load up to 4500 Fe atoms, which can also be removed to form a apoferritin with an empty intact protein cage[92].

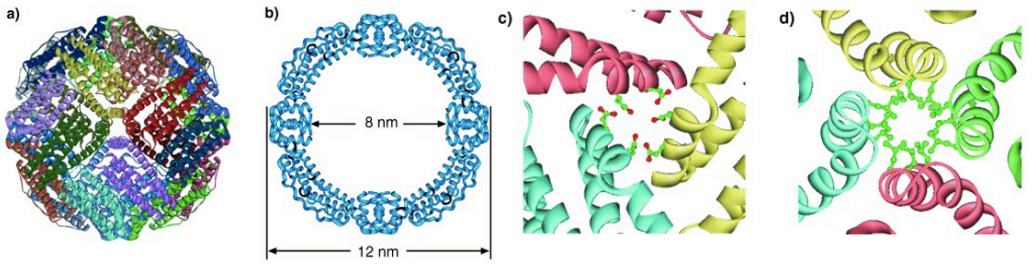

Figure 10. Representation of ferritin: a) assembled protein structure; b) inner cavity and dimension; c) hydrophilic channel; d) hydrophobic channel. Modified and reproduced with permission from the corresponding paper[93].

Apoferritin has a molecular weight (MW) of 450 kDa. In mammals, two types of subunit compose the cage: H-chain, more acid (pI = 4.8 - 5.2) and heavier (MW = 21 kDa); and L-chain, more basic (pI = 5.3 - 5.8) and lighter (MW = 19 kDa)[94]. They can be found in different ratios depending on species and organs (see Table 3). In fact, the two subunits have different functions: H-chain can bind to specific cell receptor and mediate protein internalization[95], moreover it can oxidize Fe(II) into Fe(III), by promoting its accumulation as ferrihydrite[96]. Instead, Fe nucleation is favored by L-chain.

Table 3. Approximate H- and L- chain ratio (%) of ferritin from different species and tissues. Reproduced with permission from the corresponding paper[97].

Species & organs	Human placenta	Human spleen	Human liver	Human heart	Human serum	Horse spleen	Rat liver
H-chain	20	10	50	90	0	8	35
L-chain	80	90	50	10	100	92	65

1.3.2 Function in the body

The main role of ferritin in human body concerns Fe homeostasis. The oxidative reaction enables to encapsulate massive quantity of metal ions in a minimum space, thus loaded Fe can be easily transported through the body and be rapidly available in the tissues. If Fe concentration in cytosol is higher compared to normal values, ferritin loads ions through its channel and store them. On the contrary, low levels lead to Fe release[98]. The biomineralization process can be divided in four steps: entrance, oxidation, nucleation and mineral core formation (Figure 11).

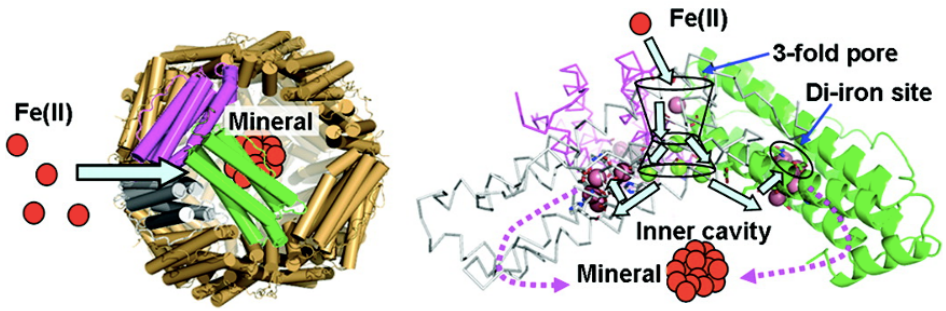

Figure 11. Biomineralization process in ferritin with a schematic representation of the trajectory of Fe(II) from outside until the formation of a mineral core inside the inner cavity. Reproduced with permission from the corresponding paper[99].

In detail, Fe(II) ions pass through 3-fold pore hydrophilic channel thanks to a ionic gradient promoted by carboxylate residues and reach the oxidoreductase site (Figure 12). Each center is embedded in the 4-helical bundles of the H-subunits, involves atoms from seven conserved residues and can bind up to two Fe simultaneously (see reaction (a) in Figure 13)[100,101].

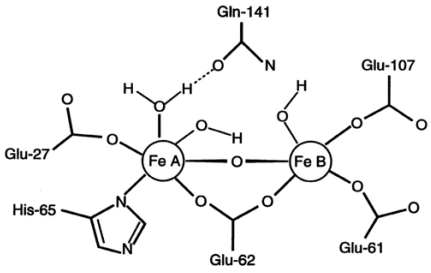

Ferritin ferroxidation

$2Fe(II) + O_2 + 4H_2O \rightarrow 2Fe(O)OH_{(core)} + H_2O_2 + 4H^+$

$2Fe(II) + H_2O_2 + 2H_2O \rightarrow 2Fe(O)OH_{(core)} + 4H^+$

Fenton reaction

$Fe(II) + H_2O_2 \rightarrow Fe(III) + OH^- + \cdot OH$

Figure 12. Ferroxidase center made of atoms from seven residues that binds two iron atoms. The site can use either O_2 or H_2O_2 to produce iron core, using the same reagents as the toxic Fenton reaction. Reproduced with permission from the corresponding paper[102].

Here 2 Fe^{2+} react with an oxygen molecule (as O_2 or H_2O_2), producing a first oxygen complex (b), converted into an intermediate (c) that is rapidly hydrolyzed in a μ-oxobridge complex (d). Successive water molecules additions give two monomeric $Fe(OH)_2^+$ ions (e) that following migrate to the cavity and nucleate starting from Fe(O)OH molecules (f). The result is a mineral core of ferrihydrite[98].

$$a)\ Protein + 2Fe^{2+} \rightarrow Protein[Fe_2]^{4+}$$

$$b)\ Protein[Fe_2]^{4+} + O_2 \rightarrow Protein[Fe_2O_2]^{4+}$$

$$c)\ Protein[Fe_2O_2]^{4+} \rightarrow Protein[Fe_2^{6+}O_2^{2-}]^{4+}$$

$$d)\ Protein[Fe_2^{6+}O_2^{2-}]^{4+} + H_2O \rightarrow Protein[Fe_2O]^{4+} + H_2O_2$$

$$e)\ Protein[Fe_2O]^{4+} + 3H_2O \rightarrow 2[Fe(OH)_2]^{+} + 2H^{+}$$

$$f)\ 2[Fe(OH)_2]^{+} \rightarrow 2Fe(O)OH_{core} + 2H^{+}$$

Figure 13. Reaction step of biomineralization when O_2 is used to form ferrihydrite inside the core or ferritin.

Ferritin has also an antioxidant function: indeed, by sequestering the metal from the cytosol, it avoids the interaction between Fe and H_2O_2, with dangerous production of free radicals via Fenton reaction (see reaction in Figure 12)[103].

1.3.3 Clinical relevance of serum ferritin

Ferritin is a protein mainly present in the cytosol, nevertheless in vertebrates it can be found also in the blood (10 - 200 μg/L)[104]. This isoform, named serum ferritin, is immunologically and morphologically similar to intracellular ferritin, with slight differences in the L-chain[105]. Its Fe loading is 4 - 20% inferior compared with cytosolic ferritin situated in liver and spleen tissues.

Serum ferritin values are frequently monitored, since they correlate with Fe body storage[106]. Low protein concentrations are found in patients with Fe-deficiency anemia, while high amount can indicate the presence of hemochromatosis or acute and chronic inflammations[107,108]. Several cells can release serum ferritin (e.g., hepatocytes, microglial cells)[109,110] as a consequence of high intracellular ferritin levels, but it was reported that macrophages are the primary source[111]. Its levels are also implemented by cells of diseased tissues, especially several kinds of tumors, for instance primary liver cancer[112], Hodgkin's lymphoma[113], breast cancer[114], gastrointestinal diseases[115], neuroblastoma[116], squamous cell carcinoma of the head and neck[117], renal cell carcinoma[118], melanoma[119] and lung cancer[120]. Normally, the abundance of this marker is associated with severe stage of the disease and a poor prognosis. Monitoring ferritin levels can also help during tumor therapy: for example, they can predict the body response to Trastuzumab treatments in women affected by $HER2^+$ breast cancer, or can provide information regarding the evolution progress of chemotherapy[121,122].

Ferritin over-expression by tumor tissues is induced by secondary effects activated in presence of a malignant formation, such as inflammation, hormonal induction, oxidative stress and hypoxia.

Indeed, it is reported that some inflammatory cytokines (e.g., tumor necrosis factor-α and interleukin-1β) can regulate ferritin transcription and translation[123,124].

Also some hormones promotes its production: both thyrotropin and insulin and have been shown to increase ferritin *in vivo*[125,126].

The protein, thanks to its ferroxidase activity, plays a fundamental role against ROS and oxidative stress. It was demonstrated that they can enhance ferritin transcription and translation, upregulating in particular the H-chain, which is responsible of the oxidation reaction. Indeed, Genetically defined electrophile response elements (EpRE) and specific iron-regulatory proteins (IRP-1 and IRP-2) control respectively ferritin transcription and translation in a time-dependent manner[127,128].

The last characteristic proper of a tumor formation that influence ferritin production is the hypoxia, that is also one of the major challenges in chemotherapy resistance[129]. For example, it was reported that hypoxia decreases IRP-1 binding activity in glial cells and enhances it in cortical neurons, resulting in a different regulation of ferritin expression[130].

1.3.4 Ferritin receptor

The mechanism of ferritin internalization in cells is receptor-mediated. In 2010 Li et *al*. demonstrated that transferrin receptor (TfR1) is exploited also by ferritin (Figure 14)[131].

Transferrin (Tf) is another example of protein with a Fe-homeostasis role in the body. It has a monomeric structure with a molecular weight of 79 kDa, and it is constituted by two lobes containing a binding site for Fe(III) each one[132]. Tf naturally circulates in the blood and can bind cells presenting TfR1. TfR1 is a transmembrane receptor with a dimer exposed on the surface of the cell. Each monomer binds one Tf with high affinity and the complex 2Tf/TfR1 is internalized with a clathrin-mediated endocytosis pathway[133].

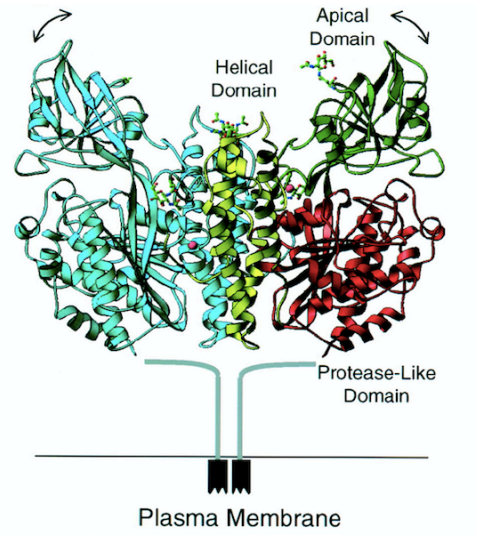

Figure 14. Crystal structure of the ectodomain of Human transferrin receptor. Reproduced with permission from the corresponding paper[134].

The same process occurs for ferritin, in particular it has been proved that the apical domain is responsible for ferritin binding. Being a larger protein, each TfR1 can bind and mediated the internalization of only one ferritin at a time[135,136].

TfR1 are abundantly expressed in cell in active proliferation, such as several kinds of tumor cells[137,138]. In particular, a study conducted in 2010 investigated nine different tumor tissues, revealing that ferritin can distinguish and prefer the binding to cancer cells, with a sensitivity of 98% and a specificity of 95% (Figure 15)[139]. These important results opened new routes for the possible clinical relevance of ferritin as nanocarrier in tumor diagnosis and therapy.

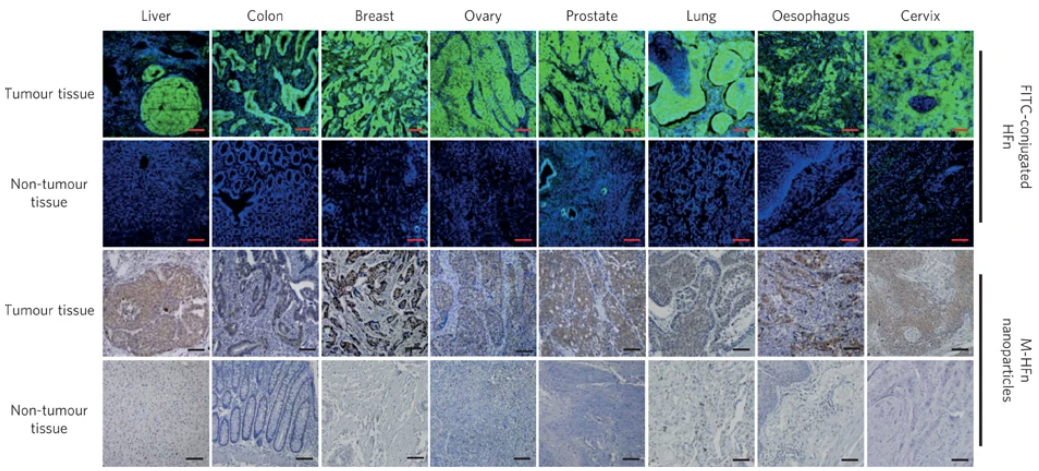

Figure 15. Tumor tissues and their corresponding normal tissues were stained by FITC-conjugated HFn protein shells and iron oxide HFn nanoparticles. Tumor tissues showed strong positive staining for iron oxide HFn nanoparticles (brown) and FITC-conjugated HFn protein shells (green fluorescence), whereas the normal and lesion tissue controls were negative for iron oxide HFn nanoparticles and FITC-conjugated HFn. Reproduced with permission from the corresponding paper[139].

1.3.5 Ferritin as nanovector

Thanks to its unique characteristics, ferritin has attracted broad interest in the nano field. The inner cavity of apoferritin is an ideal spatially restricted chemical reaction chamber, where biomineralization processes can promote artificial synthesis of homogeneous metal complexes. For example, after selective elimination of protein shell, the obtained uniform NPs can be used as nanodevices or as a template for semi-conductors production[140,141]. The encapsulation of a variety of metal ions can be exploited also for biomedical purposes: for example, FeO and Gd cores can be used as MRI CAs, copper sulfide formations are potential probe for photoacoustic imaging, while gold loaded inside ferritin have shown a cytotoxic effect especially on aggressive tumor cancer cells[142,143,144,145]. Ferritin is an ideal carrier also for several kind of molecules: for example, it can encapsulate chemotherapeutic agents, like doxorubicin and cisplatin. This promotes an efficient accumulation of active drug specifically in the tumor region, preventing side effects like cardiotoxicity[146,147]. Other examples are represented by the curcumin-like family. Despite their hydrophobic nature, such compounds can be stored in ferritin cage and be uptaken by cancer cells with unexpected therapeutic efficacy[33].

Loading process exploits two different mechanisms (Figure 16a). The first is diffusion, and it is particularly useful for ions: in particular conditions, ferritin can incorporate small elements that pass through its channels and accumulate in the cavity. The second is a process pH-

dependent: in fact, ferritin subunits are able to disassemble at extreme (low or high) pH and re-assemble with a shape memory fashion when the environmental conditions return to neutral pH[148]. If the molecules of interest are added in the buffer during such process, they will remain entrapped into the cavity at the same time as when the protein will return to its normal quaternary structure.

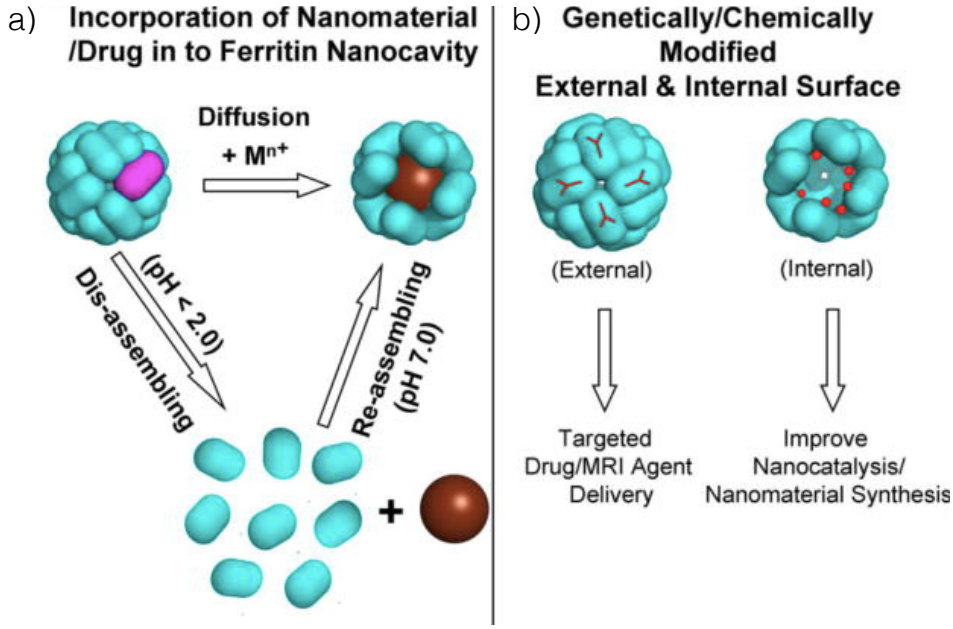

Figure 16. a) Encapsulation of nanomaterial inside ferritin nanocavity towards two different processes. b) External and internal surface modification of ferritin subunits. Reproduced with permission from the corresponding paper[149].

Moreover, the external and internal surface of ferritin can be easily genetically or chemically modified in order to further improve its selectivity (Figure 16b).

In fact, despite the natural targeting of ferritin towards cancer cells, several research groups have modified the surface of ferritin nanocages by inserting a number of target motifs, such as antibodies, peptides and antibody fragments, in order to drive NPs towards specific cells by selective recognition[150,151,152].

1.3.5 Ferritin as MRI CA

Concerning the use of ferritin for diagnosis with MRI tool, there have been published various works where the protein was exploited as nanocarrier for Gd. It has been shown that the metal can be entrapped inside the shell as free ions, forming a Gd NP with a diameter of 5 nm and a transverse relaxivity higher than the commercially available Gd-based CAs[143]. Otherwise, it can be incapsulated complexed with a chelating agent: this strategy ameliorates the safety of the compound, but the dimension of such molecules decreases the number of Gd ions loaded (10 - 35/apoferritin)[153,154]. It was also investigated the possibility to design a theranostic agent combining Gd with other molecules, for example curcumin. However, despite the results in terms of toxicity, the amount of paramagnetic ion incapsulated was insufficient to produce a good contrast[155]. Another strategy concerns the binding of Gd chelates on the outer surface of the shell (143 Gd/apoferritin), with improved results both *in vitro* and *in vivo*[156]. Given the safety challenges deriving from Gd, some researchers started investigating the entrapment of the second paramagnetic metal of election. Mn was encapsulated in ferritin for the

first time in 1995, producing an inner core of Mn(III) oxyhydroxide[157]. Being the oxidation state (II) essential to induce a paramagnetic effect, some studies were conducted to encapsulate efficiently Mn(II)[158,159]. The compounds showed R_1 values (respectively of 6.2 mM^{-1} s^{-1} and 10 mM^{-1} s^{-1}) higher than those of CAs commercially available, thus promoting the future potentialities as CA. There was also a report where a Mn loaded ferritin was tested both *in vitro* and *in vivo*, detecting a hepatocarcinoma lesion in a mouse model[160]. This latter report demonstrated the capability of such kind of CA to produce a contrast enhancement; nevertheless, liver is a clearance organ and the current CAs can easily increase the brightness in those tissues. It would have rather been worthwhile to take advantage from ferritin natural cancer specificity, in order to discover a potential effective tumor-targeted CA.

2. Aim of the work

The purpose of the present work is the development of a new CA for MRI, which possesses two important characteristics different from the conventional agents in current use: low toxicity and high selectivity for the detection of tumor lesions. Indeed, nowadays there is lack of safe CAs to improve the resolution of MRI images, with possible false positive or negative or delayed diagnosis. Usually, an MRI exam is performed without the injection of substances (Gd-based CAs), that are eventually administered for a second scan under strict restrictions: the patient must not suffer from renal issues and, in any case, the dosage should be as low as possible, since side effects and long-term accumulation of Gd in several tissues have been reported[161,162].

The design of the new nanomaterial was accurately conceived with the support of strong literature data, in order to achieve the best result. In particular, it was decided to use Mn as paramagnetic element alternative to Gd. This metal possesses five unpaired electrons compared with the seven of Gd, that are necessary to coordinate and relax water protons present in the investigated environment. Nevertheless, its natural presence and requirement in many enzymatic processes makes it a safer candidate for clinic purposes[91,71]. To overcome the theoretic lower relaxivity with respect to the standard paramagnetic metal, two strategies

have been exploited: 1) the accumulation of several Mn ions in a confined compartment; 2) the complexation with larger molecules, such as proteins. The first approach would enhance the amount of water protons that can be relaxed simultaneously in the same area, with benefits for the overall contrast in such region. The second one allows to decrease the rotational correlation time of the metal, enabling a favorable dynamic capable to provide high relaxivity[163,59,60]. Therefore, it was decided to load Mn ions inside the shell of a globular spheric protein.

Ferritin is a good candidate for several reasons: first of all, it is the ideal carrier to stably encapsulate Mn ions: its main function inside human body is Fe storage, thus it possesses a natural inclination to accumulate metal ions into its core[90]. Various studies reported examples of biomineralization reactions successfully conducted inside this protein, supporting the hypothesis of a natural tendency of ferritin to easily encapsulate Mn[164,165]. Indeed, it was demonstrated that ligand preferences and binding sites of Fe and Mn are very similar in many enzymes and, concerning ferritin, it has been discovered that Mn can bind to ferroxidase center in native ferritin influencing the efficiency of the ferroxidation reaction, while iron loading in the presence of Mn originates a core containing both metal ions[166,167,168]. The structure of the protein itself is very favorable to increase the efficiency of Mn relaxivity: in fact, thanks to the presence of different channels, water can exchange between the core and the outside favoring a rapid turnover of protons; in addition, the inner surface may enhance the relaxivity via catalytic

exchange of water protons, as already demonstrated using Gd-loaded ferritin[169]. Moreover, ferritin can target tumor lesions with high efficiency without additional functionalization thanks to one kind of its subunits: the heavy chain. In fact, it has been demonstrated that TfR1, the receptor recognizing human transferrin, is able to bind efficiently to H-ferritin subunits. Interestingly, it has also been reported that TfR1 is overexpressed in 98% of human tumor cells[138,139]. To exploit entirely the potential of this vector, H-ferritin (HFn), a recombinant variant of human apoferritin consisting of 24 self-assembled H-chain subunits, was produced and employed as carrier, since HFn can discriminate between malignant and normal cells and is preferentially internalized by cancer cells[170]. The selection of a $TfR1^+$ cancer cell line for the validation experiments would qualify this nanocomposite for the detection of a broad range of tumor lesions.

For all these reasons, the production, characterization and evaluation *in vitro* and *in vivo* of a HFn nanocomposite stably loaded with Mn ions is a relevant field of investigation.

3. Materials and methods

3.1 Production of HFn in E. coli and purification

The production of heavy chain apoferritin (HFn) was carried out following a protocol set up in our lab[170]. Briefly, Escherichia coli BL21(DE3) strain was transformed with pET30b/HFn plasmid and grown at 37 °C in Luria Bertani kanamicin medium until optical density $(OD)_{600nm}$ = 0.6. Then, the cells were induced with 0.5 mM of isopropyl β-D-1-tiogalactopiranoside (IPTG) for 2 h and 30 min. After they were collected, washed with phosphate buffered saline (PBS), and resuspended in a in lysis buffer with lysozyme and DNase I. After the sonication, the crude extract was heated at 70 °C for 15 min and centrifuged. The supernatant was loaded onto diethylaminoethanol (DEAE) Sepharose anion exchange resin, pre-equilibrated with 2-(N-Morpholino)ethanesulfonic acid potassium salt (K-MES) 20 mM, pH 6.0. In order to elute the purified protein, a stepwise NaCl gradient was used. The fractions were analyzed by Sodium Dodecyl Sulphate - PolyAcrylamide Gel Electrophoresis (SDS-PAGE) using 12% (v/v) polyacrylamide gels. Various step of washing with PBS were carried out using Amicon filter (100 kDa MWCO) to obtain pure HFn. The concentration and the purity of the solution were checked measuring the absorbance at 280 nm and the absorbance ratio 260/280 respectively with a UV-vis spectrometer.

3.2 Synthesis of Mn@HFn-RT and Mn@HFn-HT

HFn was washed with three volumes of 4-(2-hydroxyethyl)-1-piperazineethanesulfonic acid (HEPES) 20 mM pH 7.5 using Amicon filter (100 kDa MWCO) in order to exchange the protein buffer. Then, 2 mg of HFn were added to a solution of HEPES 1M, pH 8.25, to obtain a final volume of 1.44 mL. 60 µL of $MnCl_2$ 450 mM were slowly added to the solution (6 µL every 10 minutes). During this step the reaction temperature was set at 27 °C or 65 °C, obtaining NPs with different features named respectively Mn@HFn-RT and Mn@HFn-HT. The solution was stirred at 80 rpm during the addition of $MnCl_2$ and for the following 2 h to promote ions internalization. Then, it was centrifuged for 10 min at 3100 x g at 4 °C, to precipitate the potential HFn denaturated. To eliminate the excess of Mn from the solution the supernatant was centrifuged with Amicon filter (100 kDa MWCO) and then passed through a Zeba™ Spin Desalting Column (7 kDa MWCO) buffered with HEPES 20 mM, pH 7.5.

3.3 Characterization of Mn@HFn-RT and Mn@HFn-HT

The protein was quantified by both measuring absorbance at 280 nm and using the Coomassie Plus Protein Assay Reagent (Thermo Fisher Scientific). The correct native structure was determined by native PAGE using 6% (v/v) polyacrylamide gels colored with Coomassie Blue staining. The hydrodynamic diameter was evaluated by dynamic light scattering (DLS) analysis using a Zetasizer Nano ZS ZEN3600 from

Malvern Instruments Ltd (Worcestershire, UK). The protein was diluted in PBS, 0.1 mg/mL. The measurement occurred at 25 °C, operating at 4 mW of a HeNe 633 nm laser with a protein refractive index of 1.45, using a scattering angle of 90°. A disposable cuvette with 1 cm optical path length was used for the measurements. The results were expressed as mean ± standard deviation (SD) of three measurements. For transmission electron microscopy (TEM) analysis a FEI 120 kV tecnai G2 Spirit BioTWIN microscope with at an accelerating voltage of 120 kV was used. 2 µL of the sample (0.5 mg/mL) were deposited on a Formvar coated copper grid. After 5 min the grid was dried from the excess of solution. To stain the sample, the day after it was colored with uranyl acetate (1% in PBS, pH 7.5). The dried final sample was analyzed by TEM. The measurement of the mean diameter of the protein were obtained using ImageJ software and analyzing at least 150 HFn from three different images. To quantify the concentration of Mn in the solutions, inductively coupled plasma - optical emission spectroscopy (ICP-OES) Optima 7000 DV PerkinElmer was used: 100 µL of sample (0.1 mg/mL of HFn) was added to 0.5 mL of fresh aqua regia solution and left o/n. Thereafter, the solution was diluted with 2 mL of distilled water. Every sample was prepared and analyzed in triplicate. The results are expressed as mean ± SD.

3.4 Mn-oxidizing assay

A solution of 0.04% leucoberbeline blue dye (Sigma Aldrich) in 45 mM acetic acid (Sigma) was used to quantify oxidized Mn (Mn(III), (IV) and (VII)), as reported in literature[171]. 500 µL of the mixture were added to 100 µL of Mn@HFn-RT and Mn@HFn-HT solutions, and after 30 min the absorbance was detected with a UV-vis spectrometer at 620 nm. Standard curves were obtained from $KMnO_4$ samples (Merk).

3.5 Relaxivity studies

The values of longitudinal and transverse relaxation times of Mn@HFn-RT and Mn@HFn-HT were measured with a 0.47 T (20 MHz) Time-Domain NMR (nuclear magnetic resonance) Benchtop Systems (Bruker Minispec mq20), using respectively t1_sr_mb and t2_cp_mb sequences. The samples were analyzed using 200 µL of solution in 10 mm diameter NMR glass tubes, left in the relaxometer at 310 K. R_1 and R_2 relaxation rates were calculated as $1000/T_1$ or $1000/T_2$ respectively, while r_1 and r_2 relaxivity coincided with the angular coefficient of the calibration curve R against Mn concentration. The T_1-weighted phantom images of Mn@HFn were obtained with a 7 T MRI imaging system (Pharmascan®, Bruker BioSpin, Billerica, MA). A multi slice multi echo sequence with a repetition time of 0.4 s and an echo time of 10 ms was used. Gd-DTPA, a commercial contrast agent, was selected as positive control. Solutions with the same concentration of Mn or with the same concentration of

protein, were compared respectively. It was chosen a protein concentration equal to 0.1 mg/mL.

3.6 Electron paramagnetic resonance analysis

Samples of Mn@HFn-RT, Mn@HFn-HT, $MnCl_2$ and $MnCl_2$ in HEPES 20 mM heated for 2 h at 65 °C were prepared. Electron paramagnetic resonance studies were carried out using a Bruker EMX spectrometer operating in X-Band, with a frequency modulation of 100 kHz, 0.2 – 63 mW of microwave power, magnetic field modulation of 5-10 Gauss and equipped with an Oxford cryostat operating in a range of temperatures between 4 and 298 K. Spectra were registered either at 130 K. The signal intensity of the samples was normalized to allow a comparison between the spectra.

3.7 Cell lines

HCC1954 and HeLa, human tumor cell lines respectively from mammary gland and cervix were used as $TfR1^+$ model of cancer cells, while the murine fibroblasts NIH-3T3 were selected as healthy cell line. HCC1954 cells were cultured in Dulbecco's Modified Eagle's Medium (DMEM) supplemented with 10% fetal bovine serum, 2 mM L-glutamine, penicillin (50 IU/mL) and streptomycin (50 mg/mL), while HeLa and NIH-3T3 medium was composed by Roswell park memorial institute (RPMI) supplemented with 10% fetal bovine serum, 2 mM L-glutamine, penicillin (50 IU/mL) and streptomycin (50 mg/mL). Cells were maintained at 37 °C

in humidified atmosphere containing 5% CO2 and sub-cultured prior to confluence using trypsin/EDTA.

3.8 TfR1 expression

3×10^5 cells were immunodecorated in flow cytometry tubes with anti-uPAR antibody (3 µg/tube; ADG3937, Sekisui, MA, USA) in phosphate buffered saline (PBS), 1% Bovine Serum Albumin (BSA; Sigma) for 30 min at RT. Then, cells were washed thrice with PBS and immunodecorated with Alexa Fluor 647 goat anti-mouse secondary antibody (3 µg/tube; A-21235 Thermo Fisher Scientific, MA, USA) in PBS, 2% BSA and 2% goat serum for 30 min at RT. After three washes with PBS, cells were analyzed by flow cytometry. 10^4 events were acquired for each analysis, after gating on viable cells and on singlets. The data (median fluorescence intensity) were normalized against the untreated sample and expressed as mean ± SD of 3 independent replicates. Cells immunodecorated with the secondary antibody only were used as control.

3.9 Cell viability assay

HeLa cells, a $TfR1^+$ model of tumor cells, were cultured on a 96 multiwell dish at a density of 5×10^3 cells/well and grown for 24 h in Dulbecco's Modified Eagle's Medium (DMEM) supplemented with 10% fetal bovine serum, 2 mM L-glutamine, penicillin (50 IU/mL) and streptomycin (50 mg/mL). Then, cells were incubated with Mn@HFn-RT or Mn@HFn-HT,

with a concentration of HFn equal to 0.1 mg/mL. After 24 h, 48 h and 72 h respectively, cells were washed with PBS and then incubated for 3 h at 37 °C with 0.1 mL of 3-(4,5-dimethyl-2-thiazolyl)-2,5-diphenyl- 2H-tetrazolium bromide (MTT) stock solution previously diluted 1:10 in DMEM medium without phenol red. After incubation, 1 mL of MTT solubilizing solution was added to each well to solubilize the MTT formazan crystals (Promega). Absorbance was read using a testing wavelength of 570 nm and a reference wavelength of 620 nm. The results are expressed as mean ± standard error (SE) of six individual experiments normalized on untreated cells.

3.10 Kinetics of Mn release

Mn@HFn-RT solution and a control batch with the same amount of free Mn and HFn were stored in two dialysate devices and kept in HEPES 20 mM pH 7.5 under shaking. At the desired time points (30 min, 1 h, 2 h, 3 h, 4 h, 18 h, 26 h), the dialysis buffers were analyzed with the relaxometer Bruker Minispec mq20 to calculate the shift of T_1 relaxation time. The experiment was conducted in triplicate and the results are expressed as mean ± SD.

3.11 Cellular binding assay by flow cytometry

FITC-Mn@HFn-RT was prepared incubating 5 mg of Mn@HFn-RT (2 mg/mL) with 1 mg of fluoresceine isothiocyanate (FITC, Sigma) (2 mg/mL) in $NaHCO_3$ 0.1 M for 2 h under stirring. Then, the solution was

passed through a Zeba™ Spin Desalting Column (7 kDa MWCO) to remove the excess of FITC. HCC1954 and NIH-3T3 cells (3×10^5) were incubated for 45 min at 4 °C in flow cytometry tubes in the presence of 0.05 mg/mL of FITC-Mn@HFn-RT alone or with 1 mg/mL of transferrin. After incubation, cells were washed three times with PBS. Labeled cells were resuspended with 0.3 mL of PBS-EDTA 2 mM and analyzed by CytoFLEX flow cytometry (Beckman Coulter). 1×10^4 events were acquired for each analysis, after gating on single cells, and a sample of untreated cells was used to set the appropriate gate on the region of positivity. The data reported the % of positive cells as mean ± standard deviation (SD) of three individual experiments. Untreated cells were used as control.

3.12 Cellular uptake assay by flow cytometry

HCC1954 and NIH-3T3 were cultured on 12 well plate until sub-confluence and incubated with 0.1 mg/mL of FITC-Mn@HFn-RT for different time periods (1, 5 and 24 h). After two steps of washing with PBS, cells were detached with tripsin/EDTA, washed three times again with PBS and finally resuspended with 0.3 mL of PBS-EDTA 2 mM. Samples were analyzed by CytoFLEX flow cytometry (Beckman Coulter). 1×10^4 events were acquired for each analysis, after gating on single cells, and a sample of untreated cells was used to set the appropriate gate on the region of positivity. The data reported the % of positive cells

as mean ± standard deviation (SD) of three individual experiments. Untreated cells were used as control.

3.13 Cellular uptake by immunodecoration and confocal detection

3×10^5 HCC1954 cells were cultured on cover glass slips precoated with polylysine and, after 24 h, incubated with 0.1 mg/mL of FITC-Mn@HFn-RT suspended in complete medium. Then, cells were washed PBS, fixed with 4% paraformaldehyde (37 °C, 20 min) and then subjected to membrane and nucleus staining by incubation with Wheat Germ Agglutinin (WGA)-Alexa Fluor 555 conjugate (1 μg/mL) and 4',6-diamidin-2- phenylindole (DAPI) (1 μg/mL), respectively. After washing with PBS, cover slips were mounted with ProLong Antifade reagent (Thermo Fisher Scientific, MA, USA) and examined by Nikon A1 Confocal Microscope (Nikon Instruments) equipped with laser excitation lines 405, 488 and 555 nm. Images were acquired at 1024 × 1024 pixel resolution and with a 63 × magnification oil-immersion lens. In order to confirm the correct setup of FITC channel, an untreated sample was as well analyzed, and no signal was found.

3.14 Cellular uptake by ICP - OES

1.5×10^6 HCC1954 cells were plated and the day after they were incubated with 0.1 mg/mL of Mn@HFn-RT for 30 h. Then, cells were washed five times with PBS, detached with tripsin/EDTA and counted.

After a final step of wash with PBS, cells were collected, resuspended in 0.2 mL of PBS and digested with 2 mL of aqua regia for 72 h. After the addition of further 0.4 mL of distilled water, the samples were analyzed by inductively coupled plasma optical emission spectroscopy (ICP-OES) Optima 7000 DV PerkinElmer. Each sample was measured three times and the results are expressed as mean ± SD.

3.15 Relaxivity studies *in vitro*

HeLa cells were plated on a 6 multiwell dish at a density of 5 x 10^5 cells/cm and grown for 24 h. The day after they were incubated with a solution of Mn@HFn-RT (0.1 mg/mL of HFn) for 24 h. Thereafter, the cells were collected, washed with PBS and resuspended in 250 µL of media. To avoid cell precipitation during the relaxometer analysis, 250 µL of pre-heated Matrigel were mixed with the cells and placed in a 10 mm diameter NMR glass tubes to solidify. Then, they were analyzed with the relaxometer Bruker Minispec mq20. Each sample was prepared in triplicate and the results are expressed as mean ± SD.

3.16 Animals

For MRI *in vivo* acquisitions, six nude mice were maintained in a fully equipped facility and their conditions were observed daily. Animals were cared according to the guidelines of the Italian Ministry of Health. All experiments were conducted under an approved protocol (authorization n° 994/2016-PR). HCC1954 cells, a $HER2^+$ breast tumor cell line, were

cultured in Roswell Park Memorial Institute (RPMI) supplemented with 10% fetal bovine serum, 2 mM L-glutamine, penicillin (50 IU/mL) and streptomycin (50 mg/mL), and then implanted subcutaneously in each mouse in a mixture of 1 x 10^7 cells and Matrigel. The state of health and behaviour of each animal was observed daily, and the weight was monitored every three days, until the tumors reached a dimension around 100-200 mm^3.

3.17 MR images of Mn@HFn-RT

MR images were acquired with a Bruker Pharmascan 7.0 T on animals anesthetized with isoflurane gas. The acquisitions were performed respectively before the injection (n = 6), and 1 h (n = 3), 5 h (n = 6) and 24 h (n = 3) after a single dose of Mn@HFn-RT (50 mg/kg of HFn corresponding to 1.2 mg/kg of Mn). Then, images were analyzed, and the intensity of a muscle region was used to normalize the intensity values of tumor regions. Final results are expressed as mean ± SE.

3.18 Epifluorescence analysis of HFn-AF660 performed *in vivo* and *ex vivo*

HCC1954 cells were cultured and implanted subcutaneously in four nude mice in a mixture of 10^7 cells suspended in growth media and Matrigel. Animals were monitored and treated as described in animal section, until the tumor reached a dimension around 100-200 mm^3. To observe the biodistribution of HFn in mice body, the protein was labeled

with Alexa Fluor$_{660}$ (HFn-AF660) and injected in the tail vein of mice (5 mg/kg of HFn). PBS was used as control. Fluorescent images were obtained by placing the animals previously anesthetized with isoflurane gas in an IVIS Lumina II imaging system (Perkin Elmer) at 37 °C. The *in vivo* images were acquired after 1 h and 4 h after the NPs injection with a 720 nm emission filter, and excitation was scanned from 570 nm to 640 nm. Mice autofluorescence was removed by spectral unmixing. After *in vivo* acquisitions, mice were sacrificed, and organs were dissected and analyzed in the IVIS system. All the epifluorescence (Epf) intensity values were normalized after subtracting Epf values obtained by mice injected with PBS. Final results are expressed as mean ± SE.

4. Results and discussion

4.1 Synthesis and characterization of Mn@HFn-RT and Mn@HFn-HT

HFn was produced, purified and the good quality of each batch was assessed according to an established protocol performed in our laboratory[170]. During my master thesis I carried out several studies in order to determine the best encapsulation protocol of Mn ions inside the shell of HFn[172]. It was especially investigated the possibility to load Mn complexed with chelating agents. Briefly, among the checked molecules, it was selected the macrocyclic molecule 1,4,7,10-Tetraazacyclododecane-1,4,7,10-tetraacetic acid (DOTA) and the complex Mn-DOTA was loaded exploiting the pH-dependent process of disassembly and reassemble of HFn subunits. Many parameters were tested, but the best outcome enabled the encapsulation of just 23 Mn ions/HFn with a protein recovery rate around 48.5%.

Therefore, in the next studies performed during my Ph.D., I focused on the diffusion strategy to incorporate ions. First of all, it was decided to conduct the Mn loading reaction at constant pH values around 8/8.5, in order to maintain Mn(II) in the correct state of oxidation. In fact, during the pH-dependent encapsulation process originally performed, it was observed that pH fluctuations caused an instantaneous coloration of the

solution. To assess the proper buffer, some preliminary reactions were carried out incubating HFn with $MnCl_2$ respectively in borate, AMPSO and HEPES buffer. The latter demonstrated to be the best option, since in the other cases there were evidence of protein precipitation immediately after Mn addition (Borate buffer) or during the reaction (AMPSO buffer). The cause may be attributable to Mn unproper interaction with buffer molecules that compromised protein stability. It was selected HEPES 1M pH 8.25 during $MnCl_2$ additions and during the successive incubation time, to avoid pH fluctuations, while a less concentrated one (HEPES 20 mM) to store the final product. Furthermore, to efficiently buffer the pH in the presence of $MnCl_2$, that exhibited an acid behaviour, it was decided to incorporate $MnCl_2$ slowly inside HFn solution with 10 consecutive additions. They were tested three different concentrations of $MnCl_2$ and the best one was chosen on the basis of protein recovery rate and final Mn/HFn molar ratio. The results are reported in Table 4.

Table 4. HFn protein recovery rate and Mn/HFn ratio obtained after HFn reaction with $MnCl_2$ 150 mM, 450 mM and 1.5 M respectively.

	$MnCl_2$ 150 mM	$MnCl_2$ 450 mM	$MnCl_2$ 1.5 M
HFn recovery rate (%)	78 %	70 %	15 %
Mn/HFn molar ratio	120	218	n.d.

Summarizing, the encapsulation of Mn ions was achieved incubating $MnCl_2$ 450 mM with HFn under controlled conditions (Figure 17): 10 addictions of $MnCl_2$ every 10 min inside a solution of HFn buffered with HEPES 1M, followed by 2 h of coincubation under stirring; then, it was centrifuged for 10 min at 3100 x g at 4 °C, to precipitate the potential HFn denaturated. To eliminate Mn excess from the solution, the supernatant was centrifuged with Amicon filter and then passed through a Zeba™ Spin Desalting Column changing the buffer to HEPES 20 mM pH 7.5.

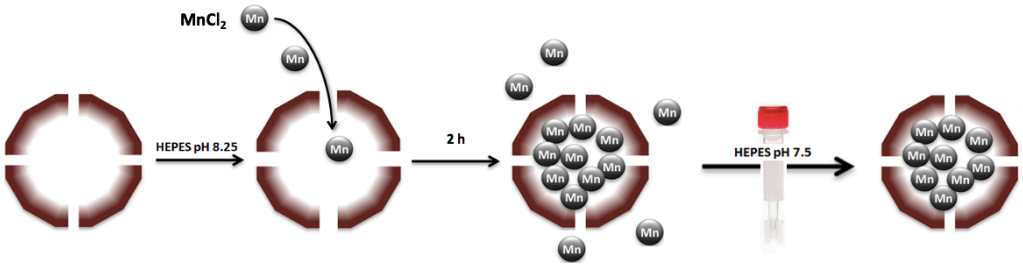

Figure 17. Mn@HFn synthesis reaction: HFn was incubated in HEPES 1M with addition of $MnCl_2$ solution to form a core of Mn ions. After 2 h of incubation, the steps of purification eliminated the undesired Mn outside the shell of the protein.

This final protocol of encapsulation was performed either at 27 °C and 65 °C, obtaining two different batches of Mn@HFn nanocomplexes, namely Mn@HFn-RT and Mn@HFn-HT, respectively. After the synthesis and purification, Mn@HFn-RT (Figure 19a) appeared as a transparent solution, while Mn@HFn-HT (Figure 19b) revealed a light brown color. The protein recovery efficiency was 70% (± 4%) for Mn@HFn-RT, while it decreased to 56% (± 12%) when the temperature was set at 65 °C, indicating also a higher reproducibility of the reaction at RT (Table 5).

Table 5. Comparison of different parameters obtained respectively between Mn@HFn-RT and Mn@HFn-HT.

	Mn@HFn-RT	Mn@HFn-HT
HFn recovery rate (%)	66 - 74	44 - 68
Mn/HFn molar ratio	185 - 251	914 - 1260
r_1 (mM^{-1} s^{-1})	25.5 - 31.1	2.3 - 3.3
r_2 /r_1	2.0 - 2.6	2.5 - 3.3

Native gel electrophoresis showed that the protein maintained the original molecular weight both in Mn@HFn-RT and Mn@HFn-HT samples (Figure 18a), and TEM analysis confirmed that the protein preserved its distinctive structure after the reaction: indeed, core-shell architecture was clearly detectable with an inner and outer effective diameter of 7.4 ± 2.2 nm and 12.1 ± 1.4 nm respectively (Figure 18b).

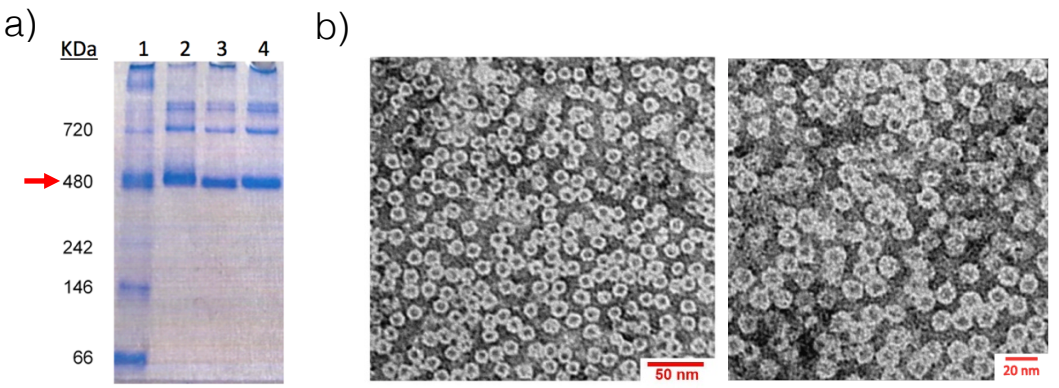

Figure 18. a) Native polyacrylamide gel 6% (v/v). Samples have been loaded in the following order: 1) marker, 2) HFn, 3) Mn@HFn-RT and 4) Mn@HFn-HT. b) TEM image of Mn@HFn-RT at two different zooms.

The hydrodynamic diameter assessed by DLS analysis (12.2 ± 0.5 nm (Figure 19a) and 13.5 ± 1.1 nm (Figure 19b), respectively) was consistent with the size reported for native ferritin (~12 nm)[90].

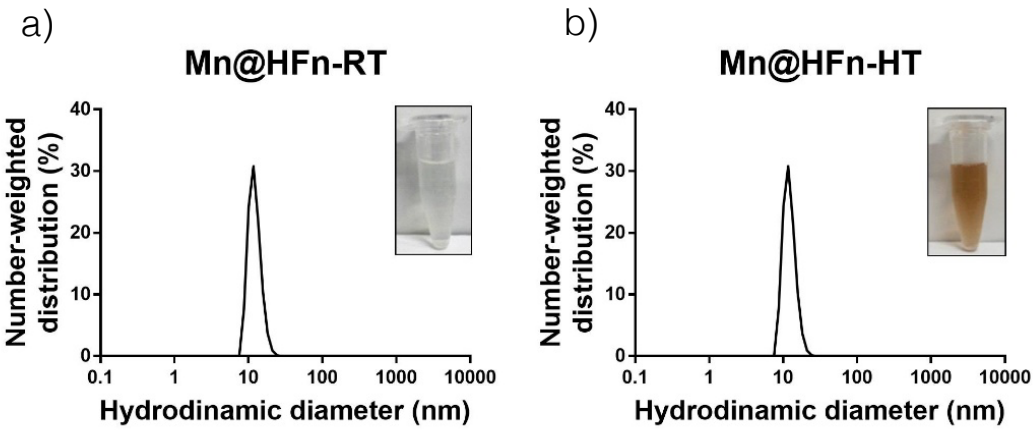

Figure 19. a) Mn@HFn-RT size distribution detected by DLS analysis and a representative sample image. b) Mn@HFn-HT size distribution detected by DLS analysis and a representative sample image.

In both samples, the data supported the hypothesis that the maintained structural integrity of HFn should be able to promote an effective recognition of TfR1 receptor and the consequent cellular uptake.

4.2 Mn encapsulation and relaxivity of Mn@HFn-RT and Mn@HFn-HT

After protein disassembly in acidic environment, Mn was quantified by ICP-OES analysis and the Mn/HFn molar ratio was estimated as 218 (± 33) for Mn@HFn-RT and 1087 (± 173) for Mn@HFn-HT (Table 4). In order

to look into the different loading efficiency recorded, multiple synthesis of Mn@HFn were repeated setting different reaction temperature parameters (27 °C, 40 °C, 50 °C and 65 °C). As showed in Figure 20, where each reaction temperature was correlated to the corresponding Mn/HFn ratio, it was found that the encapsulation rate increased with the reaction temperature.

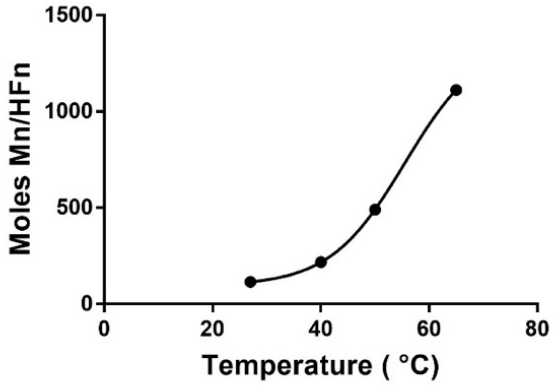

Figure 20. Correlation between Mn loading and reaction temperature.

Afterwards, the dependence of the oxidation state of Mn from the reaction conditions was assessed by a colorimetric assay[171]. Briefly, leucoberbeline complexation with Mn(III), Mn(IV) or Mn(VII) was detected at 620 nm by UV-vis spectroscopy analysis and oxidized Mn quantified by means of a calibration curve. The results (Figure 21) indicated that in Mn@HFn-RT samples Mn retained the initial oxidation state (II), while after Mn@HFn-HT synthesis it was mainly oxidized (68±14%). Taken together, if the higher reaction temperature (65 °C) improved the internalization of the Mn ions inside the protein, on the other hand it could

also have caused its partial oxidation negatively affecting the contrast power[173].

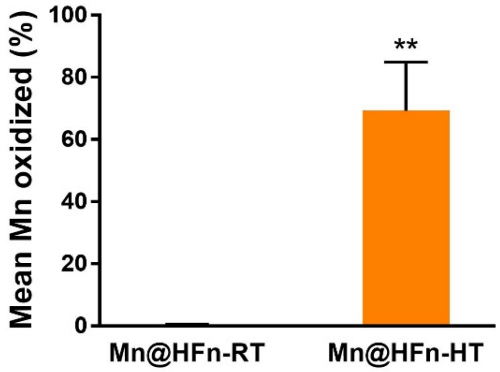

Figure 21. Quantification of the percentage of Mn oxidized in Mn@HFn-RT and Mn@HFn-HT samples. Reported values are mean ± SD (n = 3). ** $P < 0.005$ (Student's t-test).

To confirm the previous assumption, the relaxivity (r) of Mn@HFn-RT and Mn@HFn-HT was calculated after measuring the relaxation time as a function of CAs concentration. As reported in Figure 22, r_1 was found significantly higher in Mn@HFn-RT (28.3 mM^{-1} s^{-1} based on Mn concentration) than Mn@HFn-HT (2.8 mM^{-1} s^{-1}) and, considering the r_1 of approved Gd-based CAs analyzed under the same experimental conditions (e.g., Dotarem 3.4 mM^{-1} s^{-1}; Primovist 5.3 mM^{-1} s^{-1})[174], Mn@HFn-RT showed superior performance. Moreover, in this analysis, both Mn@HFn-RT and Mn@HFn-HT proved to be suitable as positive-CAs with a r_2/r_1 rate of 2.3 and 2.9, respectively[56] (Table 5). The robustness of the synthetic approach was confirmed by results reproducibility after several preparations (Table 5).

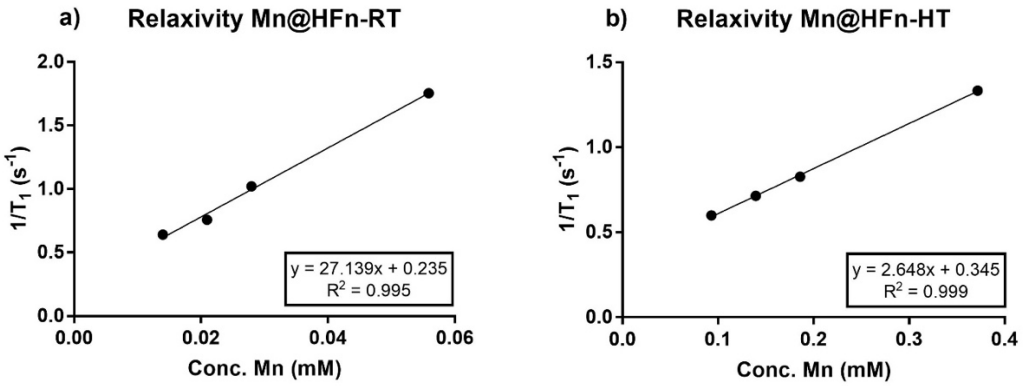

Figure 22. T_1 relaxation rate of Mn@HFn-RT (a) and Mn@HFn-HT (b) as a function of Mn molar concentration using 0.47 T NMR relaxometer. The slope of the curves expresses the transverse relaxivity (r_1).

In order to confirm the direct correlation of the lower r detected using Mn@HFn-HT compared to Mn@HFn-RT with the extent of Mn ions oxidation, an aqueous solution of $MnCl_2$ was incubated at 65 °C for 7 h and the relaxivity was monitored. The results revealed a gradual loss in relaxation power with time (Figure 23).

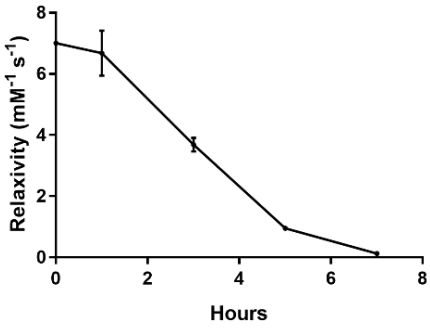

Figure 23. Relaxivity values obtained measuring the relaxation time of a solution of $MnCl_2$ left stirring at 65 °C. The solution was checked every hour with a 0.47 T NMR relaxometer. Reported values are a mean of three replicates ± SD.

The conduction of a colorimetric assay on the same sample showed a progressive and correlated increase in abundance of oxidized ions. Thus, it was possible to assert that the loss in relaxation observed in the sample was consistent with a progressive metal oxidation (Figure 24).

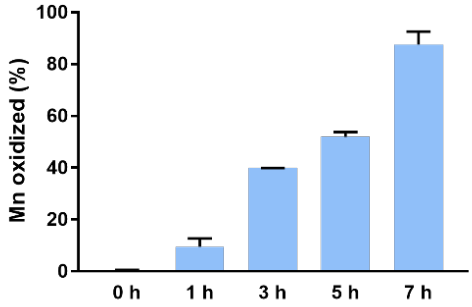

Figure 24. Leucoberbeline assay on solutions of $MnCl_2$ left stirring at 65 °C. The graph shows the percentage of Mn oxidized as a function of time. Reported values are a mean of three replicates ± SD.

Afterwards, the protein loading contribution in the relaxation was investigated by comparing the behavior of encapsulated (either Mn@HFn-RT or Mn@HFn-HT) vs. free Mn ions ($MnCl_2$) in solutions containing the same amount of metal. As shown in Figure 25, a variation in the relaxation time was detected in both HFn samples. Notably, Mn oxidation negatively affected the relaxivity of Mn@HFn-HT, whereas the Mn entrapment in Mn@HFn-RT induced a substantial decrease in T_1 value leading to enhanced relaxivity. The improved performance of the latter sample could be explained supposing that the metal complexation induced a different interaction between Mn(II) and water: indeed, it has been reported that CAs dynamics significantly affect the relaxivities[59].

For this reason, protein binding to paramagnetic metal ions was already exploited to improve CAs efficiency by slowing molecular tumbling and promoting a fast exchange rate of the coordinated water molecules[60].

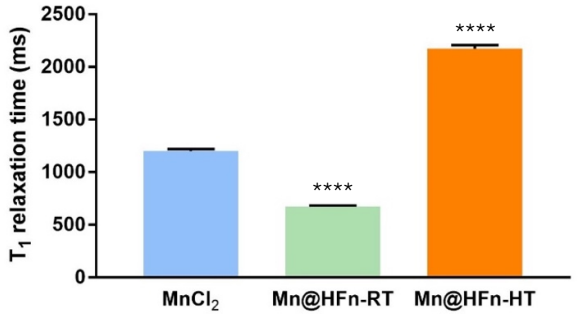

Figure 25. T_1 relaxation time measured with a 0.47 T NMR relaxometer of three different solutions containing the same amount of Mn ions. Reported values are a mean of three replicates ± SD. **** $P < 0.0001$ (Student's t-test) vs $MnCl_2$.

T_1-weighted images of Mn@HFn-RT and Mn@HFn-HT were then acquired with a 7 T MRI imaging system using a Gd-based CAs as reference. At the same concentration of paramagnetic metal (0.1 mM), Mn@HFn-RT displayed the brightest signal even compared to the clinically approved Gd-DTPA (Figure 26a). However, this experiment, likewise the above collected data, was not enough to establish the superiority of Mn@HFn-RT over Mn@HFn-HT in terms of CAs power. Since the injectable protein amount is actually the limiting factor in *in vivo* applications, it is also useful to compare these CAs in terms of HFn concentration rather than Mn ion dosage. Thus, the latter experiment was repeated normalizing the sample on HFn concentration.

As reported in Figure 26b, under this condition, Mn@HFn-RT and Mn@HFn-HT were almost equivalent in brightness. This probably happened because the lower relaxivity power of Mn in Mn@HFn-HT was balanced by the higher encapsulation efficiency of this formulation. Indeed, despite the Mn oxidation, the absolute amount of Mn(II) in Mn@HFn-RT and Mn@HFn-HT was comparable and hence the contrast ability was reasonably similar.

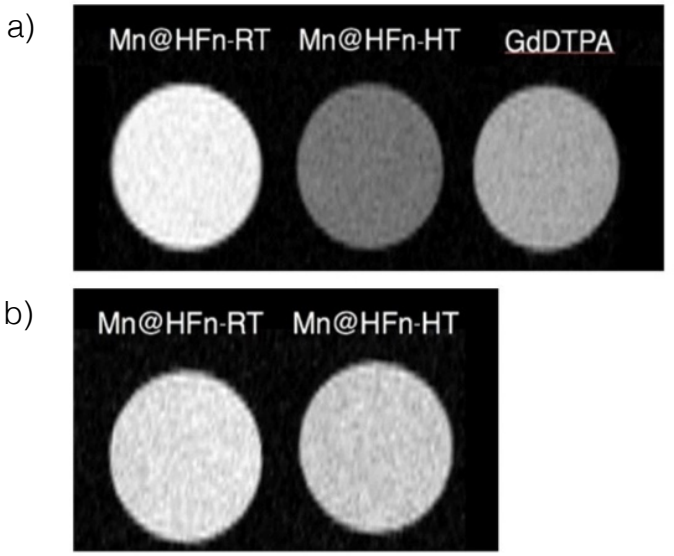

Figure 26. a) T_1-weighted images of Mn@HFn-RT, Mn@HFn-HT and Gd-DTPA obtained with the same concentration of paramagnetic metal (0.1 mM). b) T_1-weighted images of Mn@HFn-RT and Mn@HFn-HT obtained using the same concentration of HFn (0.1 mg/mL).

4.3 Characterization of the manganese core

To better characterize the samples, TEM images of Mn@HFn-RT and Mn@HFn-HT were acquired without uranyl-acetate staining. With this technique it was possible to investigate the inner core exclusively[175]. Comparing the image of empty HFn with the ones loaded with Mn, there was an evident difficulty to focus the microscope in the control sample because of its low electron density (Figure 27e). On the contrary, it was possible to observe well-defined spots when the shell incorporated Mn, particularly in Mn@HFn-HT (Figure 27a and Figure 27c). To confirm that the dots were given by the metal core, Mn@HFn-RT and Mn@HFn-HT were analyzed with a double concentration of HFn, and an effective increment of spots correlated with the amount of protein was visible (Figure 27b and 27d). The results suggested that Mn was well entrapped inside the protein shell and, when loaded at 65 °C, it assumed a conformation which produced a high electron density.

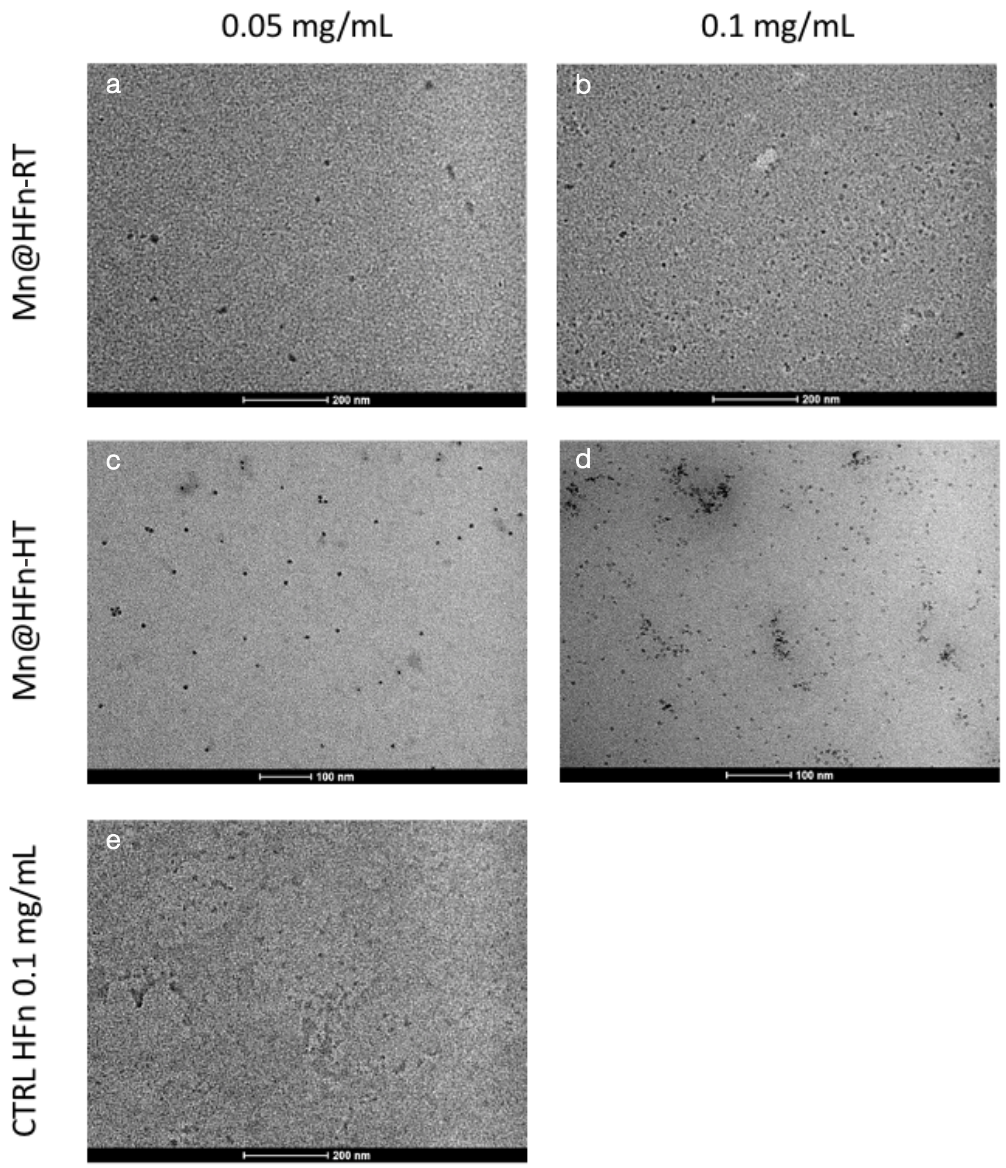

Figure 27. TEM images of unstained samples. The representative images of a) Mn@HFn-RT (0.05 mg/mL of HFn); b) Mn@HFn-RT (0.1 mg/mL of HFn); c) Mn@HFn-HT (0.05 mg/mL of HFn); d) Mn@HFn-HT (0.1 mg/mL of HFn); e) HFn (0.1 mg/mL of HFn).

Successively, an electron paramagnetic resonance experiment was conducted to obtain information concerning Mn complexation. Mn@HFn-RT and Mn@HFn-HT were analyzed, and solutions of $MnCl_2$ left at RT ($MnCl_2$-RT) or heated for 2 h at 65 °C ($MnCl_2$-HT) were used as controls. The buffer of all the sample was HEPES 20 mM, and the intensity of the spectra was normalized to allow a comparison. Both Mn@HFn-RT and $MnCl_2$-RT displayed the presence of six clearly resolved resonance lines centered at g = 2.0 with hyperfine coupling constant of about 95 G (Figure 28). These features were consistent with a Mn(II) complex in an octahedral or distorted octahedral arrangement. In particular, Mn(II) ions rotational freedom was restricted probably due to the coordination with the two nitrogen atoms from the piperazine moieties of HEPES in $MnCl_2$-RT sample, while, in the case of Mn@HFn-RT, due to the coordination with the protein functionalities. Thus, the coordination sphere of Mn(II) appeared very similar for both Mn@HFn-RT and $MnCl_2$-RT. However, the samples subjected to the heating step enabled a discrimination between their behaviors. In fact, the spectral features of $MnCl_2$-HT displayed a remarkable drop in the intensity and almost disappear, while those of Mn@HFn-HT showed an appreciable increase. These results seemed to suggest a more stable complexation of Mn(II) species by the protein, also slightly promoted by the temperature increase.

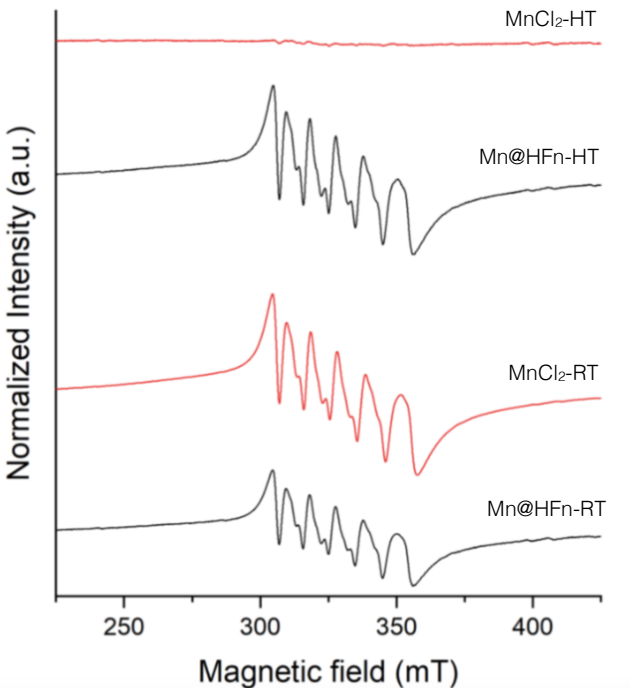

Figure 28. EPR spectra at 130 K of Mn@HFn-RT, Mn@HFn-HT, and solutions of $MnCl_2$ left at RT ($MnCl_2$-RT) or heated for 2 h at 65 °C ($MnCl_2$-HT). All the samples were in HEPES 20 mM buffer.

4.4 Cell viability

As required prior to the *in vivo* experiments, the cellular toxicity of Mn@HFn nanocomplexes was investigated. It was conducted a preliminary study by flow cytometry to assess the expression of TfR1 on two human tumor cell lines respectively from mammary gland and cervix: HCC1954 and HeLa. Both demonstrated to possess high levels of receptor, in particular HeLa cells (Figure 29).

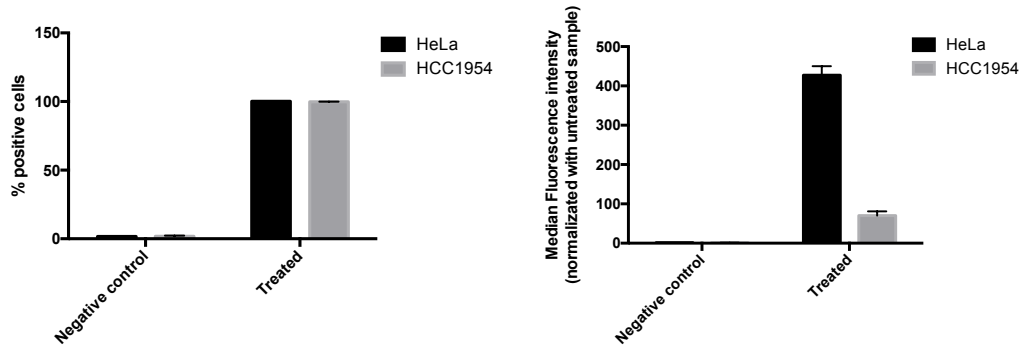

Figure 29. TfR1 expression in HeLa and HCC1954 cells evaluated by flow cytometry after double antibody immunostaining. Cells immunodecorated with the secondary antibody only were used as control. Reported values are the mean ± SD (n = 3).

HCC1954 cells were chosen as TfR1-expressing cell line to conduct further *in vitro* and *in vivo* experiments, nevertheless it was decided to investigate the viability in the presence of the nanocomposite also of HeLa cells, to be aware of possible side effects in cells presenting extremely high tendency to uptake HFn. For this purpose, the viability assay was performed incubating both cell lines with Mn@HFn-RT and Mn@HFn-HT at the same protein concentration (0.1 mg/mL) and the cellular viability was evaluated at 24, 48 and 72 h. Unloaded HFn was used as control to assess any protein nanocarrier-related effect, whereas $MnCl_2$ was tested at two different concentrations corresponding to the Mn ions amount contained in Mn@HFn-RT and Mn@HFn-HT samples (32 μM and 174 μM, respectively). According to ISO 10993-5, percentages of cell viability above 80% are considered as non-cytotoxicity; within 80%–60% weak; 60%–40% moderate and below 40% strong cytotoxicity

respectively[176]. The results showed in Figure 30 revealed that in both cell lines the viability was slightly affected by Mn@HFn-RT while in cells incubated with Mn@HFn-HT the cellular toxicity was significantly higher. This effect could be attributable to increased metal concentration, which could alter the normal cell cycle. The latter hypothesis was confirmed comparing this data with the controls (HFn and $MnCl_2$): indeed, the protein itself didn't impair the cellular growth, while free Mn(II) ions displayed a concentration-dependent effect on cell viability. It was interesting also to analyze the differences between the two cell lines: HCC1954 displayed constant values over the time, that are above 85% for Mn@HFn-RT and around 50% for Mn@HFn-HT. Instead, HeLa cells were more affected by the two nanocomposites at 24 h (75% and 43%, respectively), and the values improved over the time reaching 94% and 66% at 72 h. It was possible that the higher amount of TfR1 caused an increased uptake in the first hours, provoking a more pronounced toxicity, that might produce a cell response with a consequent amelioration with time. Altogether, these results pointed out that, despite the encapsulation reaction conducted at higher temperature remarkably increased the Mn ion loading efficacy, Mn@HFn-HT did not improve the contrast power compared to Mn@HFn-RT, in contrast it exhibited a more pronounced negative implications on cell viability. Therefore, the non-cytotoxic Mn@HFn-RT was selected as the most promising CAs nanocomplex and the next experiments were thus conducted with this sample.

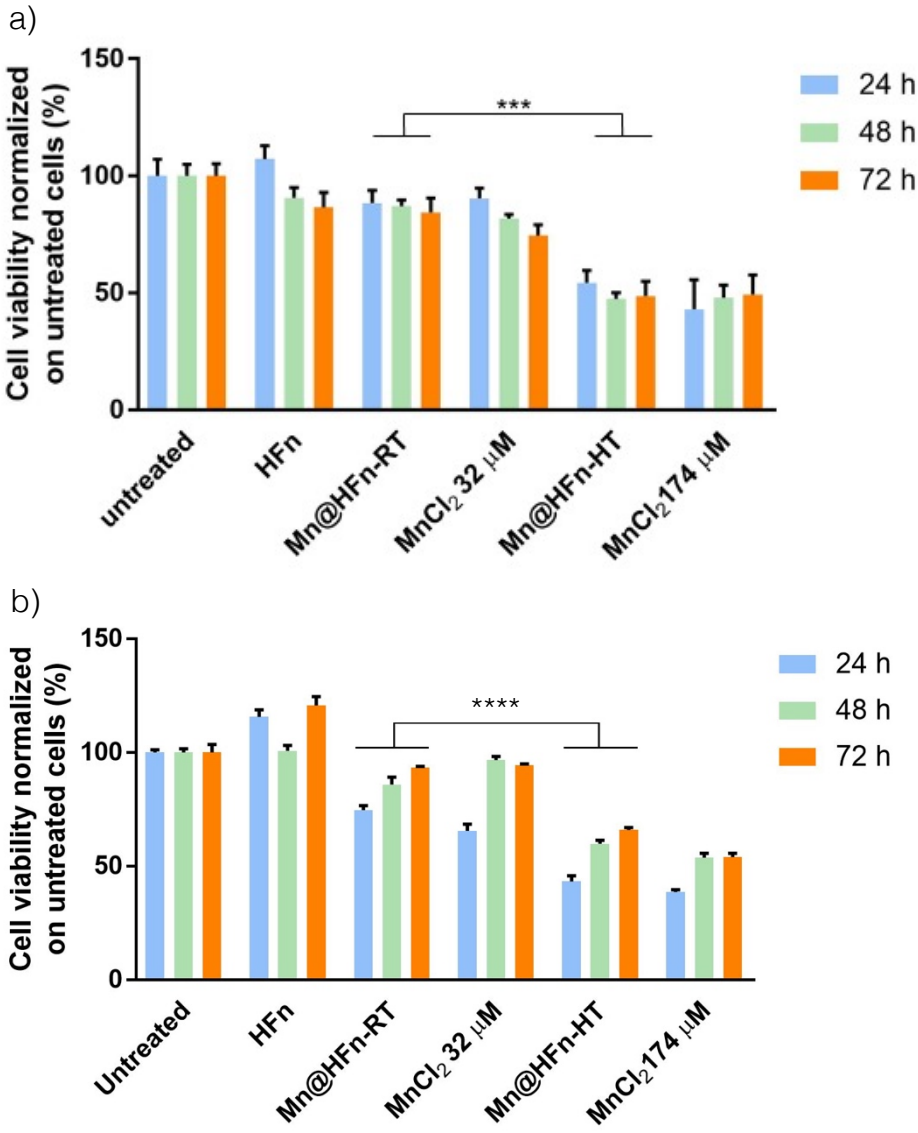

Figure 30. Cell Viability of TfR1-expressing cells (a) HCC1954 and (b) HeLa, treated with Mn@HFn-RT (0.1 mg/mL of HFn), Mn@HFn-HT (0.1 mg/mL of HFn), free protein (0.1 mg/mL of HFn) and free Mn^{2+} (32 µM and 174 µM of $MnCl_2$). The values are the mean ± SE (n = 6) normalized on cell proliferation of untreated cells. *** P = 0.0001; **** P < 0.0001 (Student's t-test).

4.5 Study of Mn@HFn-RT contrast power stability

Mn@HFn-RT stability in aqueous solution was checked under different incubation conditions. Briefly, aliquots were kept at 4 °C, RT, 37 °C, or 37 °C with the addition of 10% fetal bovine serum (FBS) and the relaxation time was monitored every day for one week (Figure 31a). The incubation at 4 °C proved to be the best option to maintain the Mn@HFn-RT relaxivity unaltered. In contrast, an increase in temperature contributed to slightly enhance the relaxation time, with consequent decrease in relaxivity. Interestingly, when kept at 37 °C in the presence of FBS, a situation more similar to the physiological environment, the magnetic properties of the nanocomplex were more robust and the relaxation power was stably maintained for a week. It should be mentioned that the lower value observed in the first time point of FBS incubating samples was due to the different medium rather than to a change in the nanocomplex relaxivity: indeed, T_1 relaxation time of HEPES buffer with or without FBS is 3370 ± 70 ms and 3730 ± 80 ms, respectively. Overall, this data suggested that the developed Mn nanoformulation was moderately stable and this assumption was further confirmed when the best storage condition was investigated. Indeed, after three weeks at 4 °C or -20 °C, the relaxation time of the encapsulated Mn was not significantly affected (Figure 31b).

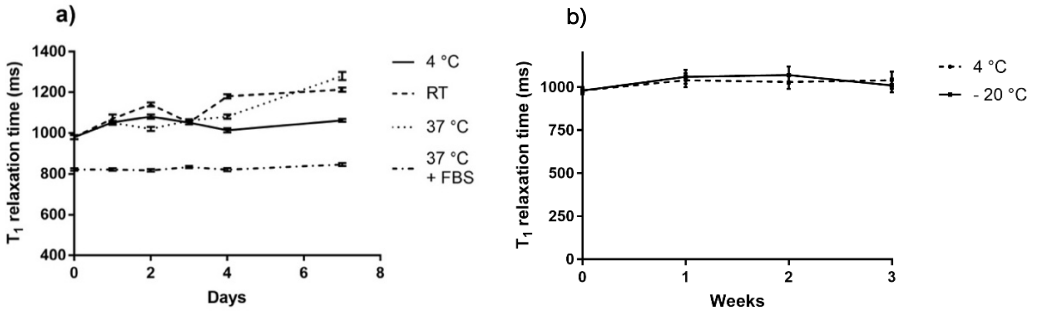

Figure 31. a) T_1 relaxation time measured with a 0.47 T NMR relaxometer on Mn@HFn-RT samples left for one week respectively at 4 °C, RT, 37 °C and 37 °C in the presence of FBS 10%. Each point is the average of two samples measured twice ± SD. b) T_1 relaxation time measured with a 0.47 T NMR relaxometer on Mn@HFn-RT samples left for three weeks respectively at 4 °C and -20 °C. Each point is the average of two samples measured twice ± SD.

Finally, a study was conducted to assess the possible release of Mn from Mn@HFn-RT. Considering the issues experienced in separating free from the encapsulated Mn, the experiment was performed exploiting the dialysis principle. At pre-determined time points, aliquots of the dialysate (the buffer outside the dialysis membrane) were withdrawn and T_1 relaxation time was measured. The decrease of the latter value is an indirect indication of Mn that passed through the dialysis membrane after being released by HFn. To rule out any interference given by interaction between the protein and the free metal ions, a solution with the same moles of HFn and Mn(II) was used as a control ($MnCl_2$ + HFn). As reported in Figure 32, the two dialysates exhibited a significant difference already in the first hours. Their gap was even more evident after 24 h, where the relaxation time of Mn@HFn-RT dialysate was 3130 ± 40 ms,

while in the dialysate of $MnCl_2$ + HFn it decreased until 2510 ± 30 ms. Although we observed an initial slight decrease, T_1 relaxation time of Mn@HFn-RT dialysate maintained constant values over time, whereas, in the $MnCl_2$ + HFn sample, the reduction trend was more pronounced and continuous. Taken together, T_1 relaxation time of Mn@HFn-RT did not change substantially because the metal was unable to move freely, suggesting an effective and stable entrapment inside the core of the protein. However, it should be noted that the decrease in T_1 relaxation time of $MnCl_2$ + HFn dialysate was not as high as observed when $MnCl_2$ was tested (~950 ms), indicating that the protein was able to interact with the metal ions to some extent.

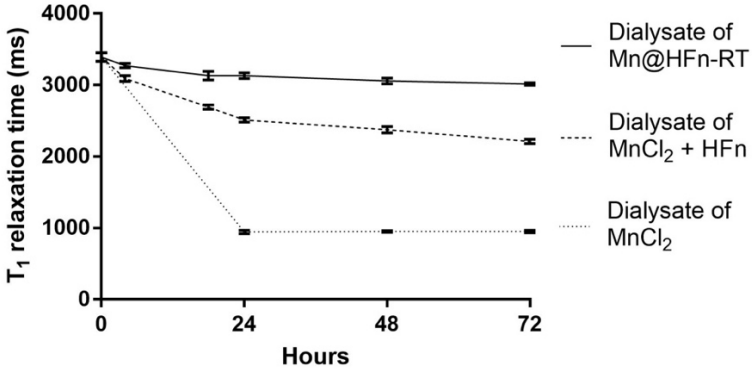

Figure 32. Mn release test in HEPES buffer 20 mM performed with a 0.47 T NMR relaxometer. Dialysate $MnCl_2$, Mn@HFn-RT and a mix of HFn and $MnCl_2$ and were checked, and T_1 relaxation time was expressed as a function of time. Each point is the average of four measurements ± SD.

4.6 *In vitro* cellular binding and uptake of Mn@HFn-RT

If the previous data demonstrated that the Mn-based contrast enhancer showed superior contrast ability compared to the approved products and long-term stability in physiological solution, the next objective was to establish the Mn@HFn-RT capability to be internalized selectively by $TfR1^+$ cells. Firstly, it was performed a flow cytometry analysis primarily investigating its binding efficiency (Figure 33). Mn@HFn-RT labeled with FITC (FITC-Mn@HFn-RT) was incubated at 4 °C for 45 min with either HCC1954 cells or $TfR1_{low}$ cell line (NIH-3T3), used as a negative control[177]. The experiment was conducted with FITC-Mn@HFn-RT alone or in the presence of the competitor transferrin (Tf). The nanocomplex concentration was adjusted to avoid reaching 100% positive cells in HCC1954 samples to better appreciate the difference between the different cell lines. The results revealed that the nanocomplex bound to the cell membrane was significantly higher in HCC1954 cells (38.4%) compared to NIH-3T3 cells (3.5%) and that in the former sample the binding capability decreased when coincubating the cells with Tf (27%), indicating that TfR1 played a fundamental role in the process. However, an incomplete inhibition was observed with Tf, likely attributable to the fast recycling of TfR1[178]. An additional hypothesis is that the multivalent HFn had a higher chance to bind TfR1 compared to the monovalent Tf[179].

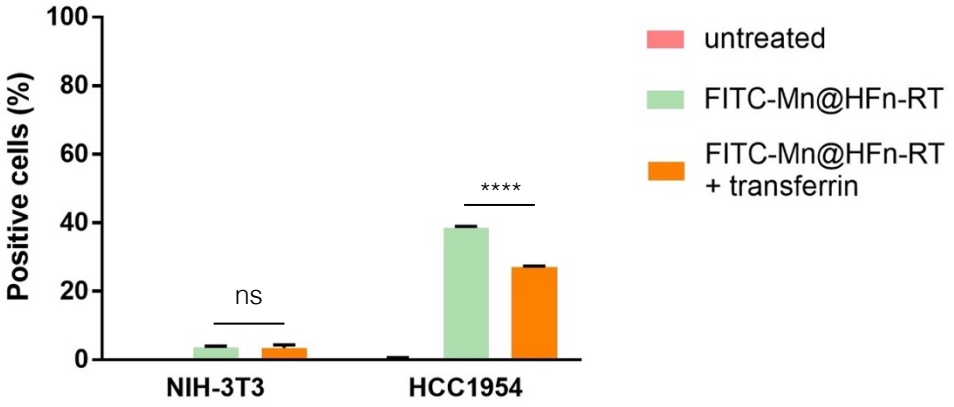

Figure 33. NIH-3T3 and HCC1954 cells were incubated with FITC-Mn@HFn-RT (0.05 mg/mL) with or without transferrin (1 mg/mL) for 45 min at 4 °C and then processed with flow cytometry (n = 3). Data represent the percentages of cells in the positive region and the values are the mean ± SD (n = 3). **** $P < 0.0001$ (Student's t-test).

Next, another experiment was conducted to measure the uptake of FITC-Mn@HFn-RT, incubating the nanocomplex at 37 °C with seeded cells and analyzing them at different time points (1, 5, 24 h) by flow cytometry. The results showed in Figure 34 confirmed the selective uptake of Mn@HFn-RT by cells overexpressing the TfR1 receptor (i.e., HCC1954 cells), and the time dependence of the process.

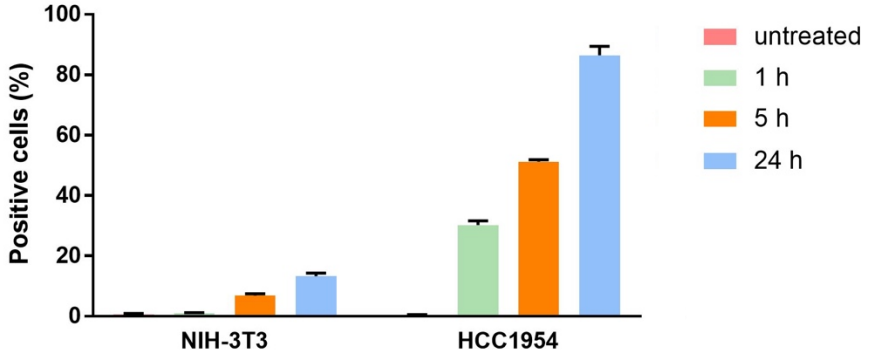

Figure 34. NIH-3T3 and HCC1954 cells were incubated with FITC-Mn@HFn-RT (0.1 mg/mL) at different time points at 37 °C and then processed with flow cytometry (n =3). Data represent the percentages of cells in the positive region and the values are the mean ± SD (n = 3).

Since the flow cytometry signal may indicate both cellular binding and internalization, the same experiment was performed with confocal microscopy, where the uptake of FITC-Mn@HFn-RT by HCC1954 cells was finally confirmed. In fact, the green spots generated by FITC emission signal were abundantly presented only inside treated cells (Figure 35). Moreover, to prove that the protein was also able to bring the metal content inside the cells, an ICP-OES experiment measured the Mn abundance in HCC1954 cells incubated with Mn@HFn-RT for 24 h. Despite the intracellular level of Mn is finely controlled and may not reflect exactly the actual amount of delivered metal, the Mn content found in the treated sample (11.6 ng of Mn/million cells ± 0.72) was 7.3 times higher than the value recorded for untreated cells (1.58 ng of Mn/million cells ± 0.19), suggesting a substantial intake of Mn ions upon cell exposure to Mn@HFn-RT.

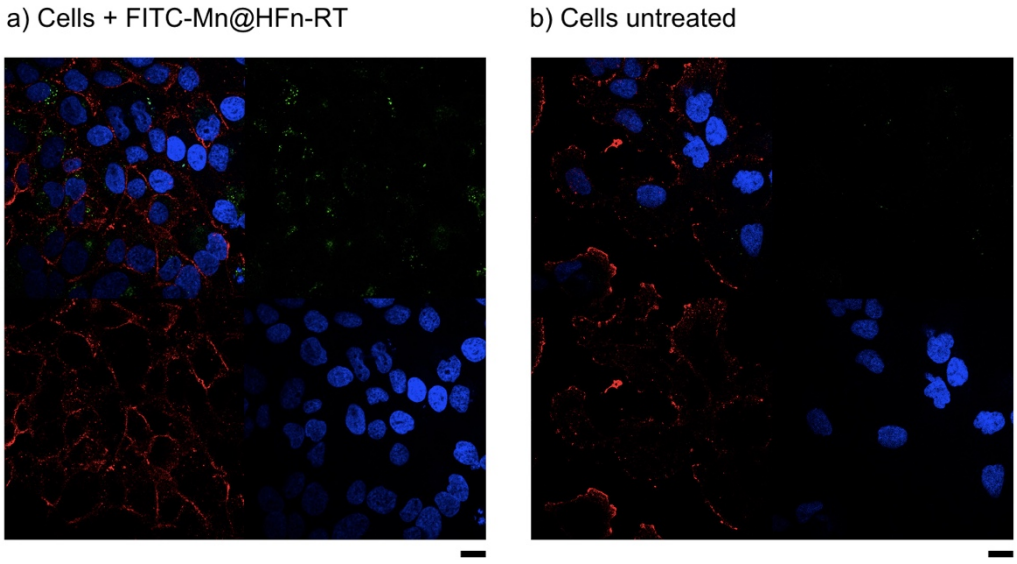

Figure 35. Representative confocal image of HCC1954 cells untreated (b) or incubated (a) for 5 h at 37 °C with FITC-Mn@HFn-RT (0.1 mg/mL; green). Nuclei were stained with DAPI (blue), while the cell membrane with WGA labeled with 555 Alexa (red). The scale bar corresponds to 20 μm.

4.7 Relaxivity test *in vitro*

After the evidence of Mn@HFn-RT uptake by TfR1$^+$ cells, a new kind of experiment was set up to start evaluating its potentiality as CA *in vitro*. HeLa cells were incubated with Mn@HFn-RT (0.1 mg/mL of HFn) for 24 h, then they were collected, resuspended in a solution of medium and Matrigel, and immediately inserted in a relaxometer tube before the solidification of the gel. This methodology was essential to maintain the cells suspended homogeneously inside the tube, avoiding their precipitation, to be detectable by relaxometer; however, the Matrigel semi-solid consistence provoked an overall increase of T_1 relaxation time, with values near to the detection limit, causing an evident difficulty

in detecting a possible parametric effect given by Mn@HFn-RT. Nevertheless, comparing the cells incubated with CAs with the untreated ones, it was still possible to observe a statistically significant variation in terms of T_1 relaxation time, supposedly due to the presence of Mn inside the cells (Figure 36). Despite the weak outcome attributable to the technical limitations of this last experiment, all the data previously collected ensured to continue investigating on Mn@HFn-RT.

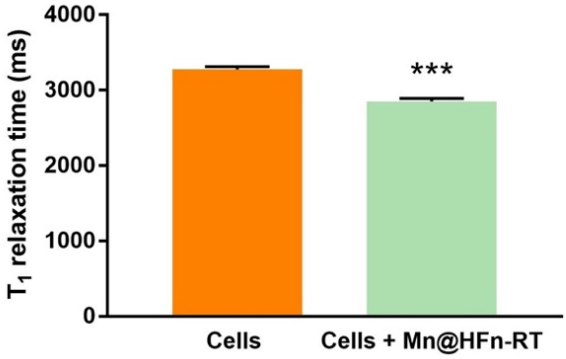

Figure 36. T_1 relaxation time of cells untreated or incubated with Mn@HFn-RT for 24 h. The results are the mean of three experiments ± SD. *** $P < 0.005$ (Student's t-test).

4.8 *In vivo* imaging of cancer lesions with Mn@HFn-RT

Thanks to the encouraging results obtained *in vitro*, it was possible to establish the Mn@HFn-RT CA efficacy *in vivo*. To this aim, HCC1954 breast cancer cells were subcutaneously inoculated into six nude mice. When the tumors reached size reached in the range 100-200 mm^3, mice were intravenously injected with Mn@HFn-RT (50 mg/kg of HFn; 1.2

mg/kg of Mn) and T_1-weighted images acquired at pre-determined time points (pre-injection, 1, 5 and 24 h post injection).

The signal intensity (SI) of the tumor region was measured, normalized versus the one detected in proximal muscle, and the brightness variation was evaluated versus the images captured before the treatment (PRE). As pointed out by the representative images in Figure 37, the tumor mass and their borders were well defined and recognizable especially 1 h after the administration of Mn@HFn-RT.

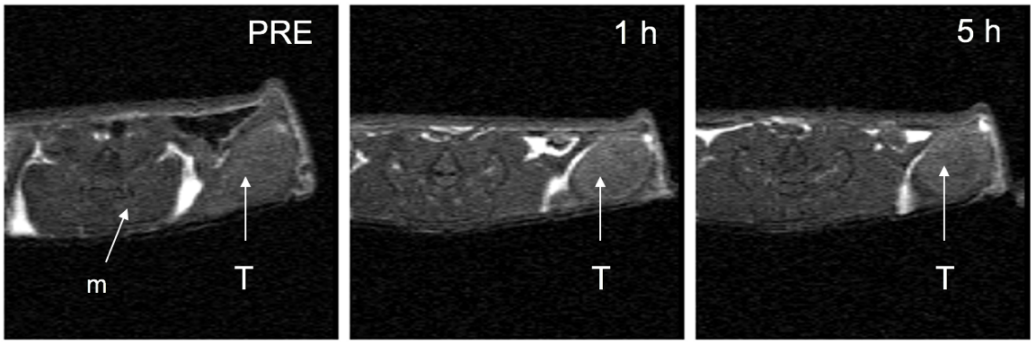

Figure 37. Representative T_1-weighted MRI images of a mouse acquired respectively before (PRE) and after (1 h and 5 h) the injection of Mn@HFn-RT (50 mg/kg of HFn). The arrows indicate the muscle (m) and the tumor (T) region.

The visual evidence was further confirmed by the quantification of the signals (Figure 38) where a significant enhancement (+25% vs. the pre-injection value) was observed at the first time point, and the tumor brightness progressively decreased with time becoming negligible at 24 h. These results suggested that HFn was efficiently accumulated in the tumor region and Mn was able to produce a hyperintense signal, facilitating the identification of cancerous lesions.

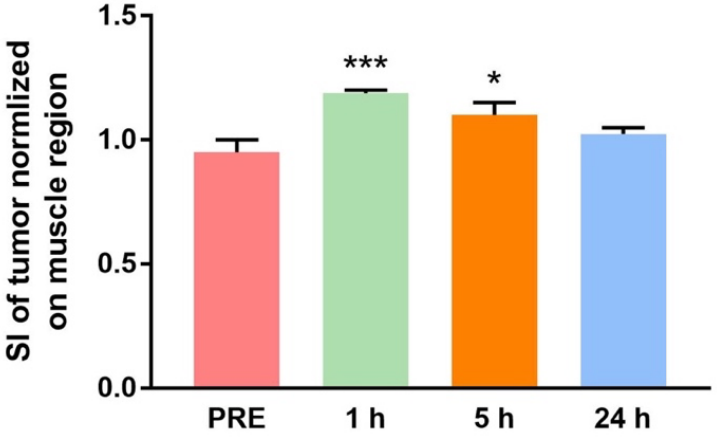

Figure 38. Intensity of the bright signal quantified in the tumor region normalized on the brightness of the muscle. The values are the mean of at least three mice ± SE. * P < 0.05; *** P < 0.005 (Student's t-test) vs PRE.

The effectiveness of Mn@HFn-RT CA was even more surprising considering the modest amount of Mn injected (1.2 mg/kg) and the fact that the enhancement concerned a tumoral tissue. Indeed, as reported in literature for Mn based nano-CAs, dosages comparable to Mn@HFn-RT (0.5 – 3 mg/kg of Mn) were used to monitor the efficiency of CAs in clearance organs (liver, kidney or bladder[180,181,83,160]). When the contrast enhancement was checked in tumor regions, the administered doses required to get a clearly detectable signal was usually almost 5-7 times higher[182]. For example, Chen et al. reported a normalized SI in a glioma bearing mice equal to 70%, after the injection of MnO-TETT-FA NPs (8 mg/kg of Mn)[85]. Also Mi et al. designed PEGMnCaP NPs able to produce an efficient SI (+60%), using a Mn administration 10 times superior compared to our experiment[183]. Two different MRI *in vivo* studies, in

which the dosages reached 25 mg/kg of Mn, were also conducted with benefit for the tumor SI of up to 30%[86] and 40%, respectively[87]. Our enhancement was around 25%, but such contrast enhancement was referred to a 20 times lower metal administration, with predictable much higher CA safety. Indeed, even if there were not certified toxic effects of Mn CAs in patients, exposure to high concentration of Mn is expected to cause side effects[88]. The unusual high efficiency of Mn@HFn-RT in enhancing the tumor contrast compared to conventional CAs could be attributable to the particular structural features of our nanocomplex, including the elevated intrinsic relaxivity (28.3 mM^{-1} s^{-1}), which allowed few atoms of Mn to produce a strong relaxation process, the dimensions of the nanocomposite (~12 nm), favorable to promote EPR passive accumulation in the tumor region[38], and the high affinity of HFn for TfR1 receptor, which also fostered active targeting to cancer cells[139].

4.9 Biodistribution evaluation of Mn@HFn-RT

In a previous work[184], the biodistribution studies conducted using a different tumor model revealed that HFn was mainly cleared by liver and kidneys, and thus it was decided to monitor the SI also in these organs.

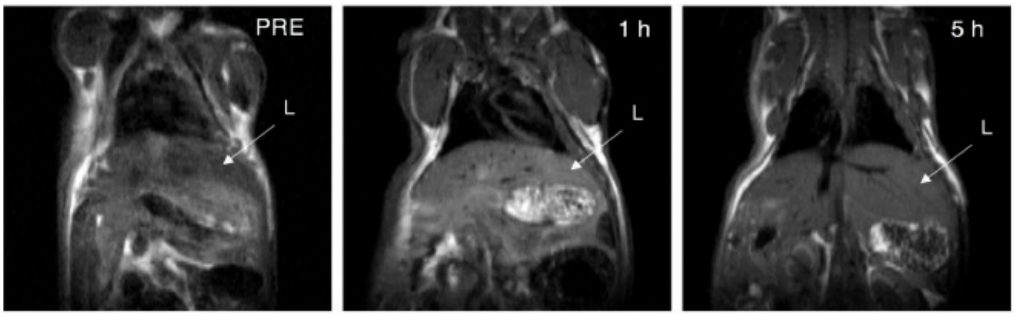

Figure 39. Representative T_1-weighted MRI images of a mouse acquired before (PRE) and after (1 h and 5 h), respectively, the injection of Mn@HFn-RT. The arrows indicate the liver (L).

Notably, in the liver (Figure 39 and 40a), after an initial strong contrast enhancement (ca. +60% vs. PRE) at 1 h post injection, the SI decreased drastically at 5 h (+20% vs. PRE), while in kidneys the enhancement was maintained at the same levels over time (around +40% at 5 h vs. PRE) (Figure 40b). Both the results suggested that Mn@HFn-RT was progressively eliminated and it is likely that immediately after the administration, the nanocarrier was mainly captured by the mononuclear phagocyte system, while at longer circulation times it was primarily excreted by urine.

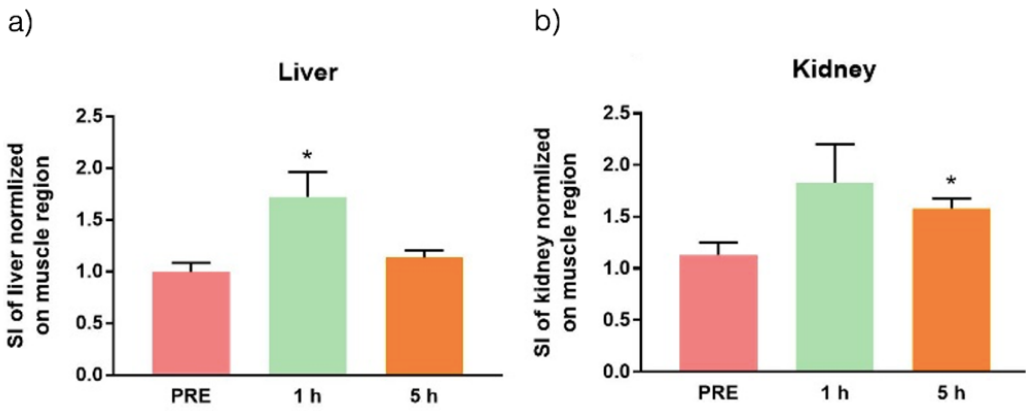

Figure 40. Intensity of the bright signal quantified in a) liver and b) kidney normalized on the brightness of the muscle. The values are the mean of at least three mice ± SE. * $P < 0.05$ (Student's t-test) vs PRE.

These data were confirmed with a final biodistribution experiment performed with fluorescent ferritin. HFn was easily functionalized with Alexa660 by coincubation and the resulting AF660-HFn was tested on mice bearing HCC1954 cells. In particular, *in vivo* epifluorescence (Epf) analysis of bladder monitored at predetermined time points after AF660-HFn i.v. injection, showed a strong Epf at 1 h, that lowered and became negligible after 24 h (Figure 41). The timing supported the investigation conducted at early time point analysis in MRI experiment, where the peak of intensity was observed after 1 h.

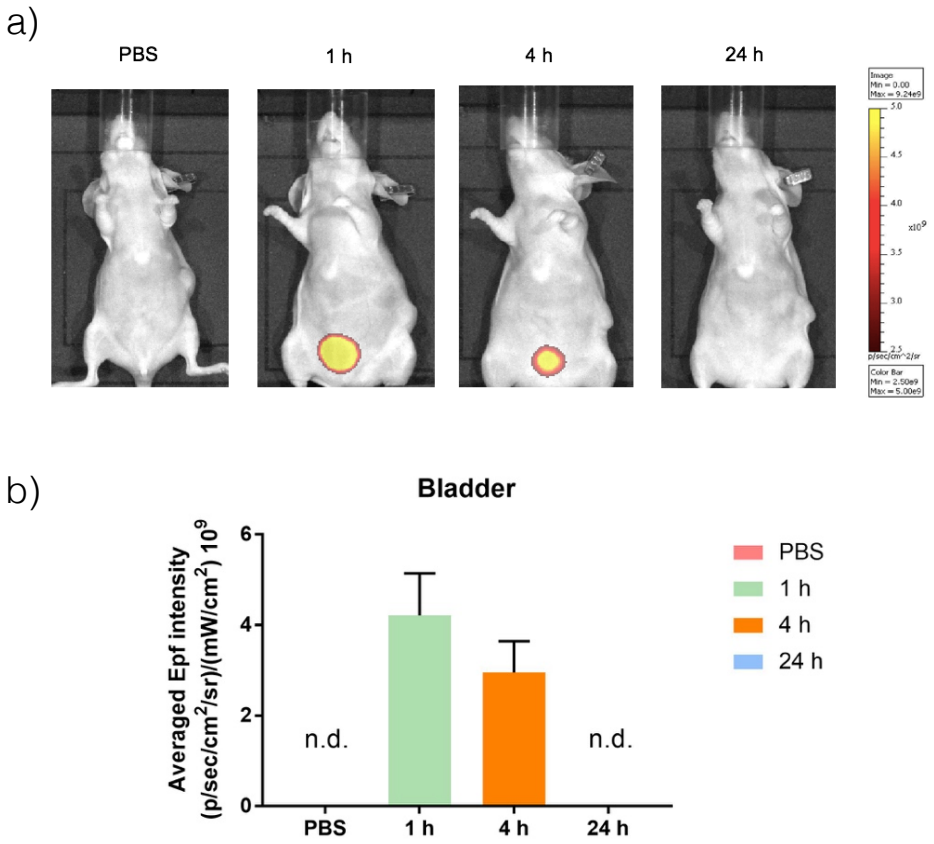

Figure 41. a) Epf images of representative mice HCC1954 tumors acquired 1 h, 4 h and 24 h after intravenous injection into the tail vein of 5 mg/kg of AF660-HFn. The color scale indicates the averaged epifluorescence expressed as radiant efficiency [(p/sec/cm^2/sr)/ (mW/cm^2)], where p/sec/cm^2/sr is the number of photons per second that leave a square centimeter of tissue and radiate into a solid angle of one steradian (sr). b) Averaged Epf intensity of the bladder region of interest (ROI). Values reported are the mean of at least three mice ± SE. PBS was administered as control. (n.d. = not detectable).

Moreover, organs dissected from mice were analyzed *ex vivo* and quantified by measuring the Epf intensity (Figure 42), and the major accumulation was observed in liver, with a discrete signal also in spleen and kidneys.

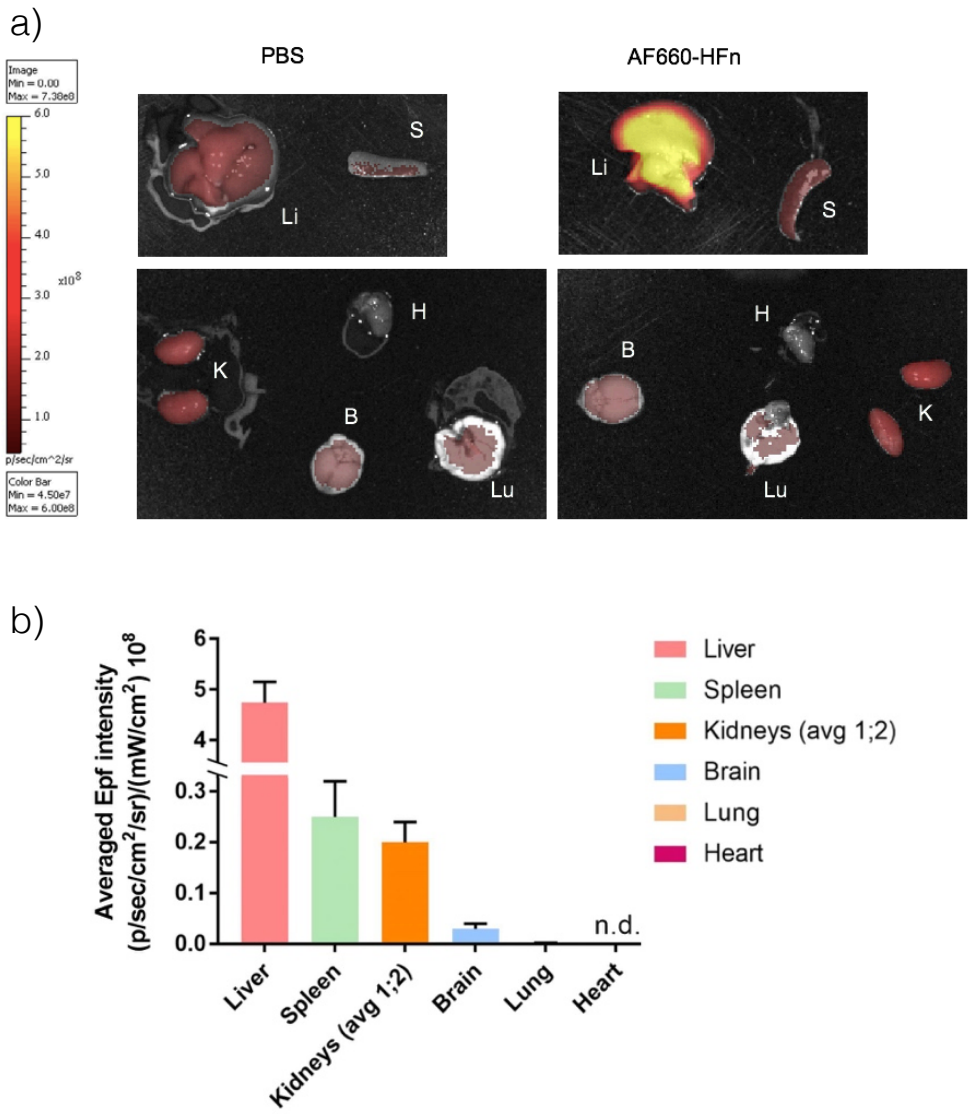

Figure 42. a) Epf of isolated spleen (S), kidneys (K), liver (L), brain (B), heart (H), lungs (Lu) after intravenous injection into the tail vein of PBS and 5 µg/kg of AF660-HFn respectively. The color scale indicates the averaged epifluorescence expressed as radiant efficiency [(p/sec/cm^2/sr)/ (mW/cm^2)], where p/sec/cm^2/sr is the number of photons per second that leave a square centimeter of tissue and radiate into a solid angle of one steradian (sr). b) Averaged Epf intensity of the ROI obtained *ex vivo* after exposure to AF660-HFn. Values reported are the mean of three mice ± SE, normalized subtracting Epf values of PBS administered as control.

Further experiments should be conducted to definitely rule out possible toxicity of Mn@HFn-RT *in vivo*, nevertheless there is evidence in support to the hypothesis that this nanocomplex was estimated to prevent important safety issues. First, the nanocarrier itself consists of a self-assembly of multiple peptide subunits derived from a protein already present in human body, thus is expected to bypass the recognition by immune system and inflammatory response. Secondly, Mn, a natural cellular constituent, is administered at very low dosages (around one order below the common dosages utilized for *in vivo* imaging of solid tumors). Finally, the rapid clearance of Mn@HFn-RT ensures an efficient excretion, also limiting possible time-dependent Mn release from the carrier, which is accounted for the main cause of side effect for conventional gadolinium-based CAs.

5. Conclusion

In summary, possible routes to obtain a powerful and non-toxic Mn-based CA for MRI were investigated. The specific aim of the research was the design and validation of an agent capable to detect malignant lesions with strong selectivity and higher sensitivity compared to most Mn- and Gd-based CAs reported so far. A protocol of biomineralization of Mn ions inside the core of HFn protein was set up at two different incubation temperatures (RT and 65 °C), and the products were characterized in terms of loading, undesired release, relaxivity, colloidal and magnetic stability, and capability to affect human cell viability. The use of HFn as an excellent biocomplexation template was justified by 1) the natural tendency of apoferritin to promote metal(II) biomineralization, and 2) by the spontaneous tumor tropism of HFn. Despite the lower encapsulation efficiency, Mn@HFn-RT was selected for further investigations because, when tested at equal HFn concentrations, it proved to be able to enhance the signal brightness at the same level of the nanocomplex obtained at 65 °C (Mn@HFn-HT), but, differently from the latter, without substantially affecting the cellular metabolic activity. Mn@HFn-RT showed superior contrast capability compared to free Mn ions, demonstrating that the metal entrapment promoted a faster water molecules relaxation. *In vitro* experiments confirmed the capability to be

bound and internalized by TfR1^{+} cells. Combining the strong contrast enhancement of Mn@HFn-RT with the expected improvement in tumor targeting due to HFn, suggested that this Mn nanocomplex could be developed for T_1-weighted MRI imaging of solid tumors. The above-mentioned results along with the higher relaxivity displayed by this new nanoformulation compared to the conventional Gd-based CAs, has enabled to explore the potential of Mn@HFn-RT for *in vivo* experiments. Noteworthy, the images obtained after injection of Mn@HFn-RT exhibited a well-defined region in correspondence of the tumor mass. This confirmed the capability of HFn to bring paramagnetic Mn(II) ions and target them properly in the tumor region. Moreover, the results indicated that a good contrast was observed with little doses of Mn, presumably minimizing possible clinical side effect. MRI experiments and biodistribution studies showed a very rapid clearance of HFn, suggesting that the best output could be achieved with an early acquisition of the images. This rapid contrast effect could avoid long waiting times for both the patients and the physicians, making Mn@HFn-RT a promising nanoCA for application in the clinical practice.

Bibliography

1. Mann, S. Life as a nanoscale phenomenon. *Angew. Chem. Int. Ed Engl.* **47**, 5306–5320 (2008).

2. Yun, Y.-H. *et al.* Tiny Medicine: Nanomaterial-Based Biosensors. *Sensors* **9**, 9275–9299 (2009).

3. Chen, F.-M. & Liu, X. Advancing biomaterials of human origin for tissue engineering. *Prog. Polym. Sci.* **53**, 86–168 (2016).

4. Pearce, A. K. & O'Reilly, R. K. Insights into Active Targeting of Nanoparticles in Drug Delivery: Advances in Clinical Studies and Design Considerations for Cancer Nanomedicine. *Bioconjug. Chem.* **30**, 2300–2311 (2019).

5. Han, X., Xu, K., Taratula, O. & Farsad, K. Applications of nanoparticles in biomedical imaging. *Nanoscale* **11**, 799–819 (2019).

6. Bose, T., Latawiec, D., Mondal, P. P. & Mandal, S. Overview of nano-drugs characteristics for clinical application: the journey from the entry to the exit point. *J. Nanoparticle Res.* **16**, 2527 (2014).

7. Zhao, Y., Sultan, D. & Liu, Y. 2 - Biodistribution, Excretion, and Toxicity of Nanoparticles. in *Theranostic Bionanomaterials* (eds. Cui, W. & Zhao, X.) 27–53 (Elsevier, 2019). doi:10.1016/B978-0-12-815341-

3.00002-X.

8. Nel, A., Xia, T., Mädler, L. & Li, N. Toxic Potential of Materials at the Nanolevel. *Science* **311**, 622–627 (2006).

9. Ha, H.-K., Kim, J. W., Lee, M.-R., Jun, W. & Lee, W.-J. Cellular Uptake and Cytotoxicity of β-Lactoglobulin Nanoparticles: The Effects of Particle Size and Surface Charge. *Asian-Australas. J. Anim. Sci.* **28**, 420–427 (2015).

10. Choi, J. *et al.* Comparison of cytotoxic and inflammatory responses of photoluminescent silicon nanoparticles with silicon micron-sized particles in RAW 264.7 macrophages. *J. Appl. Toxicol.* **29**, 52–60 (2009).

11. Li, Y., Kröger, M. & Liu, W. K. Shape effect in cellular uptake of PEGylated nanoparticles: comparison between sphere, rod, cube and disk. *Nanoscale* **7**, 16631–16646 (2015).

12. Duman, O. & Tunç, S. Electrokinetic and rheological properties of Na-bentonite in some electrolyte solutions. *Microporous Mesoporous Mater.* **117**, 331–338 (2009).

13. T. Chou, L. Y., Ming, K. & W. Chan, W. C. Strategies for the intracellular delivery of nanoparticles. *Chem. Soc. Rev.* **40**, 233–245 (2011).

14. Ali, A. *et al.* Synthesis, characterization, applications, and challenges of iron oxide nanoparticles. *Nanotechnol. Sci. Appl.* **9**, 49–67

(2016).

15. Wu, W., He, Q. & Jiang, C. Magnetic Iron Oxide Nanoparticles: Synthesis and Surface Functionalization Strategies. *Nanoscale Res. Lett.* **3**, 397–415 (2008).

16. Mahdavi, M. *et al.* Synthesis, surface modification and characterisation of biocompatible magnetic iron oxide nanoparticles for biomedical applications. *Mol. Basel Switz.* **18**, 7533–7548 (2013).

17. Jain, T. K., Reddy, M. K., Morales, M. A., Leslie-Pelecky, D. L. & Labhasetwar, V. Biodistribution, clearance, and biocompatibility of iron oxide magnetic nanoparticles in rats. *Mol. Pharm.* **5**, 316–327 (2008).

18. Gonzales-Weimuller, M., Zeisberger, M. & Krishnan, K. M. Size-dependant heating rates of iron oxide nanoparticles for magnetic fluid hyperthermia. *J. Magn. Magn. Mater.* **321**, 1947–1950 (2009).

19. Cheng, K., Peng, S., Xu, C. & Sun, S. Porous Hollow Fe3O4 Nanoparticles for Targeted Delivery and Controlled Release of Cisplatin. *J. Am. Chem. Soc.* **131**, 10637–10644 (2009).

20. Neto, L. M. M. *et al.* Specific T cell induction using iron oxide based nanoparticles as subunit vaccine adjuvant. *Hum. Vaccines Immunother.* **14**, 2786–2801 (2018).

21. Unterweger, H. *et al.* Non-immunogenic dextran-coated superparamagnetic iron oxide nanoparticles: a biocompatible, size-tunable contrast agent for magnetic resonance imaging. *Int. J.*

Nanomedicine **12**, 5223–5238 (2017).

22. Yu, J. *et al.* Smart MoS2/Fe3O4 Nanotheranostic for Magnetically Targeted Photothermal Therapy Guided by Magnetic Resonance/Photoacoustic Imaging. *Theranostics* **5**, 931–945 (2015).

23. Kumar, R. Chapter 8 - Lipid-Based Nanoparticles for Drug-Delivery Systems. in *Nanocarriers for Drug Delivery* (eds. Mohapatra, S. S., Ranjan, S., Dasgupta, N., Mishra, R. K. & Thomas, S.) 249–284 (Elsevier, 2019). doi:10.1016/B978-0-12-814033-8.00008-4.

24. Dong, X. *et al.* Doxorubicin and Paclitaxel-Loaded Lipid-Based Nanoparticles Overcome Multidrug Resistance by Inhibiting P-Glycoprotein and Depleting ATP. *Cancer Res.* **69**, 3918–3926 (2009).

25. Kulkarni, J. A., Cullis, P. R. & van der Meel, R. Lipid Nanoparticles Enabling Gene Therapies: From Concepts to Clinical Utility. *Nucleic Acid Ther.* **28**, 146–157 (2018).

26. Ramishetti, S. *et al.* A Combinatorial Library of Lipid Nanoparticles for RNA Delivery to Leukocytes. *Adv. Mater.* **32**, 1906128 (2020).

27. Pisano, C. *et al.* Clinical Trials with Pegylated Liposomal Doxorubicin in the Treatment of Ovarian Cancer. *J. Drug Deliv.* **2013**, (2013).

28. Chan, S. *et al.* Phase III trial of liposomal doxorubicin and cyclophosphamide compared with epirubicin and cyclophosphamide as first-line therapy for metastatic breast cancer. *Ann. Oncol.* **15**, 1527–1534

(2004).

29. Bulbake, U., Doppalapudi, S., Kommineni, N. & Khan, W. Liposomal Formulations in Clinical Use: An Updated Review. *Pharmaceutics* **9**, (2017).

30. Martínez-López, A. L. *et al.* Protein-based nanoparticles for drug delivery purposes. *Int. J. Pharm.* **581**, 119289 (2020).

31. Desai, N. *et al.* Increased antitumor activity, intratumor paclitaxel concentrations, and endothelial cell transport of cremophor-free, albumin-bound paclitaxel, ABI-007, compared with cremophor-based paclitaxel. *Clin. Cancer Res. Off. J. Am. Assoc. Cancer Res.* **12**, 1317–1324 (2006).

32. Battogtokh, G., Kang, J. H. & Ko, Y. T. Long-circulating self-assembled cholesteryl albumin nanoparticles enhance tumor accumulation of hydrophobic anticancer drug. *Eur. J. Pharm. Biopharm.* **96**, 96–105 (2015).

33. Pandolfi, L. *et al.* H-Ferritin Enriches the Curcumin Uptake and Improves the Therapeutic Efficacy in Triple Negative Breast Cancer Cells. *Biomacromolecules* **18**, 3318–3330 (2017).

34. Biabanikhankahdani, R., Alitheen, N. B. M., Ho, K. L. & Tan, W. S. pH-responsive Virus-like Nanoparticles with Enhanced Tumour-targeting Ligands for Cancer Drug Delivery. *Sci. Rep.* **6**, 37891 (2016).

35. Galbiati, E. *et al.* A fast and straightforward procedure for vault

nanoparticle purification and the characterization of its endocytic uptake. *Biochim. Biophys. Acta BBA - Gen. Subj.* **1862**, 2254–2260 (2018).

36. Ferrari, M. Nanovector therapeutics. *Curr. Opin. Chem. Biol.* **9**, 343–346 (2005).

37. Matsumura, Y. & Maeda, H. A New Concept for Macromolecular Therapeutics in Cancer Chemotherapy: Mechanism of Tumoritropic Accumulation of Proteins and the Antitumor Agent Smancs. *Cancer Res.* **46**, 6387–6392 (1986).

38. Fang, J., Nakamura, H. & Maeda, H. The EPR effect: Unique features of tumor blood vessels for drug delivery, factors involved, and limitations and augmentation of the effect. *Adv. Drug Deliv. Rev.* **63**, 136–151 (2011).

39. Maeda, H. The enhanced permeability and retention (EPR) effect in tumor vasculature: the key role of tumor-selective macromolecular drug targeting. *Adv. Enzyme Regul.* **41**, 189–207 (2001).

40. Hamaguchi, T. *et al.* NK105, a paclitaxel-incorporating micellar nanoparticle formulation, can extend in vivo antitumour activity and reduce the neurotoxicity of paclitaxel. *Br. J. Cancer* **92**, 1240–1246 (2005).

41. Schmidinger, M. *et al.* Pilot study with pegylated liposomal doxorubicin for advanced or unresectable hepatocellular carcinoma. *Br. J. Cancer* **85**, 1850–1852 (2001).

42. Iqbal, N. & Iqbal, N. Human Epidermal Growth Factor Receptor 2 (HER2) in Cancers: Overexpression and Therapeutic Implications. *Molecular Biology International* vol. 2014 e852748 https://www.hindawi.com/journals/mbi/2014/852748/ (2014).

43. Natali, P. G. *et al.* Structural properties and tissue distribution of the antigen recognized by the monoclonal antibody 653.40S to human melanoma cells. *J. Natl. Cancer Inst.* **67**, 591–601 (1981).

44. Li, J. *et al.* Polymer–lipid hybrid anti-HER2 nanoparticles for targeted salinomycin delivery to HER2-positive breast cancer stem cells and cancer cells. *Int. J. Nanomedicine* **12**, 6909–6921 (2017).

45. Falvo, E. *et al.* Antibody-drug conjugates: targeting melanoma with cisplatin encapsulated in protein-cage nanoparticles based on human ferritin. *Nanoscale* **5**, 12278–12285 (2013).

46. Seleci, M. *et al.* Smart multifunctional nanoparticles in nanomedicine. *BioNanoMaterials* **17**, 33–41 (2016).

47. Norton, L., Simon, R., Brereton, H. D. & Bogden, A. E. Predicting the course of Gompertzian growth. *Nature* **264**, 542–545 (1976).

48. Frangioni, J. V. New technologies for human cancer imaging. *J. Clin. Oncol. Off. J. Am. Soc. Clin. Oncol.* **26**, 4012–4021 (2008).

49. Weber, J., Haberkorn, U. & Mier, W. Cancer stratification by molecular imaging. *Int. J. Mol. Sci.* **16**, 4918–4946 (2015).

50. Longmaid, H. E. *et al.* In vivo 19F NMR imaging of liver, tumor, and abscess in rats. Preliminary results. *Invest. Radiol.* **20**, 141–145 (1985).

51. Wood, M. L. & Hardy, P. A. Proton relaxation enhancement. *J. Magn. Reson. Imaging JMRI* **3**, 149–156 (1993).

52. Na, H. B., Song, I. C. & Hyeon, T. Inorganic nanoparticles for MRI contrast agents. *Adv. Mater.* **21**, (2009).

53. Hashemi, R. H., Bradley, W. G. & Lisanti, C. J. *MRI: The Basics: The Basics*. (Lippincott Williams & Wilkins, 2012).

54. Lei, M. *et al.* Activated Surface Charge-Reversal Manganese Oxide Nanocubes with High Surface-to-Volume Ratio for Accurate Magnetic Resonance Tumor Imaging. *Adv. Funct. Mater.* **27**, 1700978 (2017).

55. Hao, D. *et al.* MRI contrast agents: Basic chemistry and safety. *J. Magn. Reson. Imaging* **36**, 1060–1071 (2012).

56. Estelrich, J., Sánchez-Martín, M. J. & Busquets, M. A. Nanoparticles in magnetic resonance imaging: from simple to dual contrast agents. *Int. J. Nanomedicine* **10**, 1727–1741 (2015).

57. De León-Rodríguez, L. M., Martins, A. F., Pinho, M. C., Rofsky, N. M. & Sherry, A. D. Basic MR relaxation mechanisms and contrast agent design. *J. Magn. Reson. Imaging JMRI* **42**, 545–565 (2015).

58. Werner, E. J., Datta, A., Jocher, C. J. & Raymond, K. N. High-

relaxivity MRI contrast agents: where coordination chemistry meets medical imaging. *Angew. Chem. Int. Ed Engl.* **47**, 8568–8580 (2008).

59. Caravan, P. Protein-Targeted Gadolinium-Based Magnetic Resonance Imaging (MRI) Contrast Agents: Design and Mechanism of Action. *Acc. Chem. Res.* **42**, 851–862 (2009).

60. Gianolio, E. *et al.* Relaxometric and Modelling Studies of the Binding of a Lipophilic Gd-AAZTA Complex to Fatted and Defatted Human Serum Albumin. *Chem. – Eur. J.* **13**, 5785–5797 (2007).

61. Nicolle, G. M., Tóth, É., Schmitt-Willich, H., Radüchel, B. & Merbach, A. E. The Impact of Rigidity and Water Exchange on the Relaxivity of a Dendritic MRI Contrast Agent. *Chem. – Eur. J.* **8**, 1040–1048 (2002).

62. Anselmo, A. C. & Mitragotri, S. A Review of Clinical Translation of Inorganic Nanoparticles. *AAPS J.* **17**, 1041–1054 (2015).

63. Senpan, A. *et al.* Conquering the Dark Side: Colloidal Iron Oxide Nanoparticles. *ACS Nano* **3**, 3917–3926 (2009).

64. Sárközi, S., Szegedi, C., Lukács, B., Ronjat, M. & Jóna, I. Effect of gadolinium on the ryanodine receptor/sarcoplasmic reticulum calcium release channel of skeletal muscle. *FEBS J.* **272**, 464–471 (2005).

65. Hambly, B. D. & dos Remedios, C. G. Responses of skeletal muscle fibres to lanthanide ions. Dependence of the twitch response on ionic radii. *Experientia* **33**, 1042–1044 (1977).

66. Weinmann, H. J., Brasch, R. C., Press, W. R. & Wesbey, G. E. Characteristics of gadolinium-DTPA complex: a potential NMR contrast agent. *AJR Am. J. Roentgenol.* **142**, 619–624 (1984).

67. Marckmann, P. *et al.* Nephrogenic systemic fibrosis: suspected causative role of gadodiamide used for contrast-enhanced magnetic resonance imaging. *J. Am. Soc. Nephrol. JASN* **17**, 2359–2362 (2006).

68. Xia, D., Davis, R. L., Crawford, J. A. & Abraham, J. L. Gadolinium released from MR contrast agents is deposited in brain tumors: in situ demonstration using scanning electron microscopy with energy dispersive X-ray spectroscopy. *Acta Radiol. Stockh. Swed. 1987* **51**, 1126–1136 (2010).

69. Gadolinium-containing contrast agents. *European Medicines Agency* https://www.ema.europa.eu/en/medicines/human/referrals/gadolinium-containing-contrast-agents (2018).

70. Foster, A. W., Osman, D. & Robinson, N. J. Metal Preferences and Metallation. *J. Biol. Chem.* **289**, 28095–28103 (2014).

71. Aschner, J. L. & Aschner, M. Nutritional aspects of manganese homeostasis. *Mol. Aspects Med.* **26**, 353–362 (2005).

72. Silva, A. C. *et al.* Detection of cortical laminar architecture using manganese-enhanced MRI. *J. Neurosci. Methods* **167**, 246–257 (2008).

73. Yu, X., Wadghiri, Y. Z., Sanes, D. H. & Turnbull, D. H. In vivo

auditory brain mapping in mice with Mn-enhanced MRI. *Nat. Neurosci.* **8**, 961–968 (2005).

74. Van Meir, V. *et al.* Differential effects of testosterone on neuronal populations and their connections in a sensorimotor brain nucleus controlling song production in songbirds: a manganese enhanced-magnetic resonance imaging study. *NeuroImage* **21**, 914–923 (2004).

75. Federle, M. P. *et al.* Safety and efficacy of mangafodipir trisodium (MnDPDP) injection for hepatic MRI in adults: results of the U.S. multicenter phase III clinical trials (safety). *J. Magn. Reson. Imaging JMRI* **12**, 186–197 (2000).

76. Drugs@FDA: FDA-Approved Drugs. https://www.accessdata.fda.gov/scripts/cder/daf/index.cfm?event=overview.process&ApplNo=020652.

77. Teslascan. *European Medicines Agency* https://www.ema.europa.eu/en/medicines/human/EPAR/teslascan (2018).

78. Small, W. C., Macchi, D. D., Parker, J. R. & Bernardino, M. E. Multisite study of the safety and efficacy of LumenHance, a new gastrointestinal contrast agent for MRI of the abdomen and pelvis. *Acad. Radiol.* **5 Suppl 1**, S147-150; discussion S156 (1998).

79. Drugs@FDA: FDA-Approved Drugs. https://www.accessdata.fda.gov/scripts/cder/daf/index.cfm?event=over

view.process&ApplNo=020686.

80. H, B. *et al.* Manganese dipyridoxyl diphosphate:: MRI contrast agent with antioxidative and cardioprotective properties? In vitro and ex vivo assessments. *Biochem. Biophys. Res. Commun.* **254**, 768–772 (1999).

81. Kim, B., Schmieder, A. H., Stacy, A. J., Williams, T. A. & Pan, D. Sensitive biological detection with a soluble and stable polymeric paramagnetic nanocluster. *J. Am. Chem. Soc.* **134**, 10377–10380 (2012).

82. Li, J., Wu, C., Hou, P., Zhang, M. & Xu, K. One-pot preparation of hydrophilic manganese oxide nanoparticles as T1 nano-contrast agent for molecular magnetic resonance imaging of renal carcinoma in vitro and in vivo. *Biosens. Bioelectron.* **102**, 1–8 (2018).

83. Hu, X. *et al.* Water-soluble and biocompatible MnO@PVP nanoparticles for MR imaging in vitro and in vivo. *J. Biomed. Nanotechnol.* **9**, 976–984 (2013).

84. Yang, H. *et al.* Silica-Coated Manganese Oxide Nanoparticles as a Platform for Targeted Magnetic Resonance and Fluorescence Imaging of Cancer Cells. *Adv. Funct. Mater.* **20**, 1733–1741 (2010).

85. Chen, N. *et al.* Folic acid-conjugated MnO nanoparticles as a T1 contrast agent for magnetic resonance imaging of tiny brain gliomas. *ACS Appl. Mater. Interfaces* **6**, 19850–19857 (2014).

86. Luo, Y. *et al.* Facile synthesis and functionalization of manganese

oxide nanoparticles for targeted T1-weighted tumor MR imaging. *Colloids Surf. B Biointerfaces* **136**, 506–513 (2015).

87. Wang, P. *et al.* Antifouling Manganese Oxide Nanoparticles: Synthesis, Characterization, and Applications for Enhanced MR Imaging of Tumors. *ACS Appl. Mater. Interfaces* **9**, 47–53 (2017).

88. Roels, H. *et al.* Epidemiological survey among workers exposed to manganese: effects on lung, central nervous system, and some biological indices. *Am. J. Ind. Med.* **11**, 307–327 (1987).

89. Addison, G. M. *et al.* An immunoradiometric assay for ferritin in the serum of normal subjects and patients with iron deficiency and iron overload. *J. Clin. Pathol.* **25**, 326–329 (1972).

90. Ford, G. C. *et al.* Ferritin: design and formation of an iron-storage molecule. *Philos. Trans. R. Soc. Lond. B Biol. Sci.* **304**, 551–565 (1984).

91. Sigel, A. & Sigel, H. Metal ions in biological systems, volume 35: iron transport and storage microorganisms, plants, and animals. *Met.-Based Drugs* **5**, 262 (1998).

92. Harrison, P. M. & Arosio, P. The ferritins: molecular properties, iron storage function and cellular regulation. *Biochim. Biophys. Acta* **1275**, 161–203 (1996).

93. Ueno, T. *et al.* Size-selective olefin hydrogenation by a Pd nanocluster provided in an apo-ferritin cage. *Angew. Chem. Int. Ed Engl.* **43**, 2527–2530 (2004).

94. Simsek, E. & Kilic, M. A. Magic ferritin : A novel chemotherapeutic encapsulation bullet. in *Journal of magnetism and magnetic materials* vol. 293 509–513 (2005).

95. Zhang, L. *et al.* H-Chain Ferritin: A Natural Nuclei Targeting and Bioactive Delivery Nanovector. *Adv. Healthc. Mater.* **4**, 1305–1310 (2015).

96. Levi, S. *et al.* Mechanism of ferritin iron uptake: activity of the H-chain and deletion mapping of the ferro-oxidase site. A study of iron uptake and ferro-oxidase activity of human liver, recombinant H-chain ferritins, and of two H-chain deletion mutants. *J. Biol. Chem.* **263**, 18086–18092 (1988).

97. Zhang, L. & Knez, M. Spherical nanoscale protein templates for biomedical applications: A review on ferritin. *J. Nanosci. Lett.* **2**, 6 (2012).

98. Chasteen, N. D. & Harrison, P. M. Mineralization in ferritin: an efficient means of iron storage. *J. Struct. Biol.* **126**, 182–194 (1999).

99. Tosha, T., Ng, H.-L., Bhattasali, O., Alber, T. & Theil, E. C. Moving Metal Ions through Ferritin–Protein Nanocages from Three-Fold Pores to Catalytic Sites. *J. Am. Chem. Soc.* **132**, 14562–14569 (2010).

100. Lawson, D. M. *et al.* Solving the structure of human H ferritin by genetically engineering intermolecular crystal contacts. *Nature* **349**, 541–544 (1991).

101. Haldar, S., Bevers, L. E., Tosha, T. & Theil, E. C. Moving Iron through Ferritin Protein Nanocages Depends on Residues throughout Each Four α-Helix Bundle Subunit. *J. Biol. Chem.* **286**, 25620–25627 (2011).

102. Arosio, P., Ingrassia, R. & Cavadini, P. Ferritins: A family of molecules for iron storage, antioxidation and more. *Biochim. Biophys. Acta BBA - Gen. Subj.* **1790**, 589–599 (2009).

103. Baldi, A. *et al.* Ferritin contributes to melanoma progression by modulating cell growth and sensitivity to oxidative stress. *Clin. Cancer Res. Off. J. Am. Assoc. Cancer Res.* **11**, 3175–3183 (2005).

104. Jacobs, A., Miller, F., Worwood, M., Beamish, M. R. & Wardrop, C. A. Ferritin in the serum of normal subjects and patients with iron deficiency and iron overload. *Br. Med. J.* **4**, 206–208 (1972).

105. Santambrogio, P., Cozzi, A., Levi, S. & Arosio, P. Human serum ferritin G-peptide is recognized by anti-L ferritin subunit antibodies and concanavalin-A. *Br. J. Haematol.* **65**, 235–237 (1987).

106. Walters, G. O., Miller, F. M. & Worwood, M. Serum ferritin concentration and iron stores in normal subjects. *J. Clin. Pathol.* **26**, 770–772 (1973).

107. Allen, K. J. *et al.* Iron-overload-related disease in HFE hereditary hemochromatosis. *N. Engl. J. Med.* **358**, 221–230 (2008).

108. Kalantar-Zadeh, K., Rodriguez, R. A. & Humphreys, M. H.

Association between serum ferritin and measures of inflammation, nutrition and iron in haemodialysis patients. *Nephrol. Dial. Transplant. Off. Publ. Eur. Dial. Transpl. Assoc. - Eur. Ren. Assoc.* **19**, 141–149 (2004).

109. Tran, T. N., Eubanks, S. K., Schaffer, K. J., Zhou, C. Y. & Linder, M. C. Secretion of ferritin by rat hepatoma cells and its regulation by inflammatory cytokines and iron. *Blood* **90**, 4979–4986 (1997).

110. Zhang, X., Surguladze, N., Slagle-Webb, B., Cozzi, A. & Connor, J. R. Cellular iron status influences the functional relationship between microglia and oligodendrocytes. *Glia* **54**, 795–804 (2006).

111. Cohen, L. A. *et al.* Serum ferritin is derived primarily from macrophages through a nonclassical secretory pathway. *Blood* **116**, 1574–1584 (2010).

112. Kew, M. C. *et al.* Serum and tumour ferritins in primary liver cancer. *Gut* **19**, 294–299 (1978).

113. Dörner, M. H., Abel, U., Fritze, D., Manke, H. G. & Drings, P. Serum ferritin in relation to the course of Hodgkin's disease. *Cancer* **52**, 2308–2312 (1983).

114. Marcus, D. M. & Zinberg, N. Measurement of serum ferritin by radioimmunoassay: results in normal individuals and patients with breast cancer. *J. Natl. Cancer Inst.* **55**, 791–795 (1975).

115. Basso, D. *et al.* Hepatic changes and serum ferritin in pancreatic

cancer and other gastrointestinal diseases: the role of cholestasis. *Ann. Clin. Biochem.* **28 (Pt 1)**, 34–38 (1991).

116. Hann, H. W. *et al.* Prognostic importance of serum ferritin in patients with Stages III and IV neuroblastoma: the Childrens Cancer Study Group experience. *Cancer Res.* **45**, 2843–2848 (1985).

117. Maxim, P. E. & Veltri, R. W. Serum ferritin as a tumor marker in patients with squamous cell carcinoma of the head and neck. *Cancer* **57**, 305–311 (1986).

118. Partin, A. W. *et al.* Serum ferritin as a clinical marker for renal cell carcinoma: influence of tumor volume. *Urology* **45**, 211–217 (1995).

119. Luger, T. A., Linkesch, W., Knobler, R. & Kokoschka, E. M. Serial determination of serum ferritin levels in patients with malignant melanoma. *Oncology* **40**, 263–267 (1983).

120. Kukulj, S. *et al.* Altered iron metabolism, inflammation, transferrin receptors, and ferritin expression in non-small-cell lung cancer. *Med. Oncol. Northwood Lond. Engl.* **27**, 268–277 (2010).

121. Alkhateeb, A. A. *et al.* Elevation in inflammatory serum biomarkers predicts response to trastuzumab-containing therapy. *PloS One* **7**, e51379 (2012).

122. Melia, W. M., Bullock, S., Johnson, P. J. & Williams, R. Serum ferritin in hepatocellular carcinoma. A comparison with alphafetoprotein. *Cancer* **51**, 2112–2115 (1983).

123. Torti, S. V. *et al.* The molecular cloning and characterization of murine ferritin heavy chain, a tumor necrosis factor-inducible gene. *J. Biol. Chem.* **263**, 12638–12644 (1988).

124. Smirnov, I. M., Bailey, K., Flowers, C. H., Garrigues, N. W. & Wesselius, L. J. Effects of TNF-alpha and IL-1beta on iron metabolism by A549 cells and influence on cytotoxicity. *Am. J. Physiol.* **277**, L257-263 (1999).

125. Ursini, M. V. & de Franciscis, V. TSH regulation of ferritin H chain messenger RNA levels in the rat thyroids. *Biochem. Biophys. Res. Commun.* **150**, 287–295 (1988).

126. Yokomori, N. *et al.* Transcriptional Regulation of Ferritin Messenger Ribonucleic Acid Levels by Insulin in Cultured Rat Glioma Cells. *Endocrinology* **128**, 1474–1480 (1991).

127. Cairo, G. *et al.* Induction of ferritin synthesis by oxidative stress. Transcriptional and post-transcriptional regulation by expansion of the 'free' iron pool. *J. Biol. Chem.* **270**, 700–703 (1995).

128. Tsuji, Y. *et al.* Coordinate transcriptional and translational regulation of ferritin in response to oxidative stress. *Mol. Cell. Biol.* **20**, 5818–5827 (2000).

129. Cosse, J.-P. & Michiels, C. Tumour hypoxia affects the responsiveness of cancer cells to chemotherapy and promotes cancer progression. *Anticancer Agents Med. Chem.* **8**, 790–797 (2008).

130. Irace, C. *et al.* Divergent modulation of iron regulatory proteins and ferritin biosynthesis by hypoxia/reoxygenation in neurones and glial cells. *J. Neurochem.* **95**, 1321–1331 (2005).

131. Li, L. *et al.* Binding and uptake of H-ferritin are mediated by human transferrin receptor-1. *Proc. Natl. Acad. Sci. U. S. A.* **107**, 3505–3510 (2010).

132. Parkkinen, J., von Bonsdorff, L., Ebeling, F. & Sahlstedt, L. Function and therapeutic development of apotransferrin. *Vox Sang.* **83 Suppl 1**, 321–326 (2002).

133. Daniels, T. R., Delgado, T., Rodriguez, J. A., Helguera, G. & Penichet, M. L. The transferrin receptor part I: Biology and targeting with cytotoxic antibodies for the treatment of cancer. *Clin. Immunol. Orlando Fla* **121**, 144–158 (2006).

134. Lawrence, C. M. *et al.* Crystal Structure of the Ectodomain of Human Transferrin Receptor. *Science* **286**, 779–782 (1999).

135. Structure of the human ferritin-transferrin receptor 1 complex. https://www.esrf.eu/home/news/spotlight/content-news/spotlight/spotlight339.html.

136. Montemiglio, L. C. *et al.* Cryo-EM structure of the human ferritin-transferrin receptor 1 complex. *Nat. Commun.* **10**, 1121 (2019).

137. Gatter, K. C., Brown, G., Trowbridge, I. S., Woolston, R. E. & Mason, D. Y. Transferrin receptors in human tissues: their distribution

and possible clinical relevance. *J. Clin. Pathol.* **36**, 539–545 (1983).

138. Ponka, P., Beaumont, C. & Richardson, D. R. Function and regulation of transferrin and ferritin. *Semin. Hematol.* **35**, 35–54 (1998).

139. Fan, K. *et al.* Magnetoferritin nanoparticles for targeting and visualizing tumour tissues. *Nat. Nanotechnol.* **7**, 459–464 (2012).

140. Iwahori, K., Yoshizawa, K., Muraoka, M. & Yamashita, I. Fabrication of ZnSe nanoparticles in the apoferritin cavity by designing a slow chemical reaction system. *Inorg. Chem.* **44**, 6393–6400 (2005).

141. Kumagai, S. *et al.* Position-Controlled Vertical Growths of Individual Carbon Nanotubes Using a Cage-Shaped Protein. *Appl. Phys. Express* **3**, 015101 (2010).

142. Cai, Y. *et al.* Enhanced magnetic resonance imaging and staining of cancer cells using ferrimagnetic H-ferritin nanoparticles with increasing core size. *Int. J. Nanomedicine* **10**, 2619–2634 (2015).

143. Sánchez, P. *et al.* MRI relaxation properties of water-soluble apoferritin-encapsulated gadolinium oxide-hydroxide nanoparticles. *Dalton Trans. Camb. Engl. 2003* 800–804 (2009) doi:10.1039/b809645g.

144. Wang, Z. *et al.* Biomineralization-Inspired Synthesis of Copper Sulfide-Ferritin Nanocages as Cancer Theranostics. *ACS Nano* **10**, 3453–3460 (2016).

145. Ferraro, G. *et al.* Gold-based drug encapsulation within a ferritin

nanocage: X-ray structure and biological evaluation as a potential anticancer agent of the Auoxo3-loaded protein. *Chem. Commun. Camb. Engl.* **52**, 9518–9521 (2016).

146. Falvo, E. *et al.* Antibody-drug conjugates: targeting melanoma with cisplatin encapsulated in protein-cage nanoparticles based on human ferritin. *Nanoscale* **5**, 12278–12285 (2013).

147. Andreata, F. *et al.* Co-administration of H-ferritin-doxorubicin and Trastuzumab in neoadjuvant setting improves efficacy and prevents cardiotoxicity in HER2 + murine breast cancer model. *Sci. Rep.* **10**, 11425 (2020).

148. Kim, M. *et al.* pH-Dependent Structures of Ferritin and Apoferritin in Solution: Disassembly and Reassembly. *Biomacromolecules* **12**, 1629–1640 (2011).

149. Theil, E. C., Behera, R. K. & Tosha, T. Ferritins for Chemistry and for Life. *Coord. Chem. Rev.* **257**, 579–586 (2013).

150. Zhen, Z. *et al.* RGD-Modified Apoferritin Nanoparticles for Efficient Drug Delivery to Tumors. *ACS Nano* **7**, 4830–4837 (2013).

151. Kang, H. J. *et al.* Developing an antibody-binding protein cage as a molecular recognition drug modular nanoplatform. *Biomaterials* **33**, 5423–5430 (2012).

152. Schoonen, L. & Hest, J. V. van. Functionalization of protein-based nanocages for drug delivery applications. *Nanoscale* (2014)

doi:10.1039/c4nr00915k.

153. Aime, S., Frullano, L. & Geninatti Crich, S. Compartmentalization of a gadolinium complex in the apoferritin cavity: a route to obtain high relaxivity contrast agents for magnetic resonance imaging. *Angew. Chem. Int. Ed Engl.* **41**, 1017–1019 (2002).

154. Makino, A. *et al.* Effective encapsulation of a new cationic gadolinium chelate into apoferritin and its evaluation as an MRI contrast agent. *Nanomedicine Nanotechnol. Biol. Med.* **7**, 638–646 (2011).

155. Conti, L. *et al.* L-Ferritin targets breast cancer stem cells and delivers therapeutic and imaging agents. *Oncotarget* **7**, 66713–66727 (2016).

156. Cai, Y., Wang, Y., Zhang, T. & Pan, Y. Gadolinium-Labeled Ferritin Nanoparticles as T1 Contrast Agents for Magnetic Resonance Imaging of Tumors. *ACS Appl. Nano Mater.* **3**, 8771–8783 (2020).

157. Meldrum, F. C., Douglas, T., Levi, S., Arosio, P. & Mann, S. Reconstitution of manganese oxide cores in horse spleen and recombinant ferritins. *J. Inorg. Biochem.* **58**, 59–68 (1995).

158. Kálmán, F. K., Geninatti-Crich, S. & Aime, S. Reduction/dissolution of a beta-MnOOH nanophase in the ferritin cavity to yield a highly sensitive, biologically compatible magnetic resonance imaging agent. *Angew. Chem. Int. Ed Engl.* **49**, 612–615 (2010).

159. Sana, B., Poh, C. L. & Lim, S. A manganese–ferritin

nanocomposite as an ultrasensitive T2 contrast agent. *Chem. Commun.* **48**, 862–864 (2011).

160. Geninatti Crich, S. *et al.* Mn-loaded apoferritin: a highly sensitive MRI imaging probe for the detection and characterization of hepatocarcinoma lesions in a transgenic mouse model. *Contrast Media Mol. Imaging* **7**, 281–288 (2012).

161. Thakral, C. & Abraham, J. L. Gadolinium-induced nephrogenic systemic fibrosis is associated with insoluble Gd deposits in tissues: in vivo transmetallation confirmed by microanalysis. *J. Cutan. Pathol.* **36**, 1244–1254 (2009).

162. Kanda, T. *et al.* Gadolinium-based Contrast Agent Accumulates in the Brain Even in Subjects without Severe Renal Dysfunction: Evaluation of Autopsy Brain Specimens with Inductively Coupled Plasma Mass Spectroscopy. *Radiology* **276**, 228–232 (2015).

163. Caravan, P., Farrar, C. T., Frullano, L. & Uppal, R. Influence of molecular parameters and increasing magnetic field strength on relaxivity of gadolinium- and manganese-based T1 contrast agents. *Contrast Media Mol. Imaging* **4**, 89–100 (2009).

164. Gálvez, N. *et al.* Apoferritin as a nanoreactor for preparing metallic nanoparticles. *Comptes Rendus Chim.* **11**, 1207–1212 (2008).

165. Jolley, C. C. *et al.* Size and Crystallinity in Protein-Templated Inorganic Nanoparticles. *Chem. Mater.* **22**, 4612–4618 (2010).

166. Voevodskaya, N., Lendzian, F., Ehrenberg, A. & Gräslund, A. High catalytic activity achieved with a mixed manganese–iron site in protein R2 of Chlamydia ribonucleotide reductase. *FEBS Lett.* **581**, 3351–3355 (2007).

167. Ardini, M. *et al.* Study of manganese binding to the ferroxidase centre of human H-type ferritin. *J. Inorg. Biochem.* **182**, 103–112 (2018).

168. Smith, T. J. *et al.* Tuning the band gap of ferritin nanoparticles by co-depositing iron with halides or oxo-anions. *J. Mater. Chem. A* **2**, 20782–20788 (2014).

169. Vasalatiy, O., Zhao, P., Zhang, S., Aime, S. & Sherry, A. D. Catalytic effects of apoferritin interior surface residues on water proton exchange in lanthanide complexes. *Contrast Media Mol. Imaging* **1**, 10–14 (2006).

170. Bellini, M. *et al.* Protein nanocages for self-triggered nuclear delivery of DNA-targeted chemotherapeutics in Cancer Cells. *J. Control. Release Off. J. Control. Release Soc.* **196**, 184–196 (2014).

171. Krumbein, W. E. & Altmann, H. J. A new method for the detection and enumeration of manganese oxidizing and reducing microorganisms. *Helgoländer Wiss. Meeresunters.* **25**, 347–356 (1973).

172. Tullio, C. (2016) Sintesi e caratterizzazione di ioni manganese in nanotemplati proteici per lo sviluppo di nuovi agenti di contrasto per la risonanza magnetica, Master thesis, Università degli Studi di Milano-

Bicocca.

173. Reaney, S. H., Kwik-Uribe, C. L. & Smith, D. R. Manganese Oxidation State and Its Implications for Toxicity. *Chem. Res. Toxicol.* **15**, 1119–1126 (2002).

174. Rohrer, M., Bauer, H., Mintorovitch, J., Requardt, M. & Weinmann, H.-J. Comparison of magnetic properties of MRI contrast media solutions at different magnetic field strengths. *Invest. Radiol.* **40**, 715–724 (2005).

175. Dehner, C. *et al.* Ferritin and ferrihydrite nanoparticles as iron sources for Pseudomonas aeruginosa. *J. Biol. Inorg. Chem. JBIC Publ. Soc. Biol. Inorg. Chem.* **18**, 371–381 (2013).

176. 14:00-17:00. ISO 10993-5:2009. *ISO* https://www.iso.org/cms/render/live/en/sites/isoorg/contents/data/standard/03/64/36406.html.

177. Zong, M., Fofana, I. & Choe, H. Human and Host Species Transferrin Receptor 1 Use by North American Arenaviruses. *J. Virol.* **88**, 9418–9428 (2014).

178. Mayle, K. M., Le, A. M. & Kamei, D. T. The Intracellular Trafficking Pathway of Transferrin. *Biochim. Biophys. Acta* **1820**, 264–281 (2012).

179. Jones, S. K., Sarkar, A., Feldmann, D. P., Hoffmann, P. & Merkel, O. Revisiting the Value of Competition Assays in Folate Receptor-Mediated Drug Delivery. *Biomaterials* **138**, 35–45 (2017).

180. Chevallier, P. *et al.* Tailored biological retention and efficient clearance of pegylated ultra-small MnO nanoparticles as positive MRI contrast agents for molecular imaging. *J. Mater. Chem. B* **2**, 1779–1790 (2014).

181. Huang, H. *et al.* PEGylation of MnO nanoparticles via catechol–Mn chelation to improving T1-weighted magnetic resonance imaging application. *J. Appl. Polym. Sci.* **132**, (2015).

182. Addisu, K. D. *et al.* Bioinspired, Manganese-Chelated Alginate-Polydopamine Nanomaterials for Efficient in Vivo T1-Weighted Magnetic Resonance Imaging. *ACS Appl. Mater. Interfaces* **10**, 5147–5160 (2018).

183. Mi, P. *et al.* A pH-activatable nanoparticle with signal-amplification capabilities for non-invasive imaging of tumour malignancy. *Nat. Nanotechnol.* **11**, 724–730 (2016).

184. Mazzucchelli, S. *et al.* Nanometronomic treatment of 4T1 breast cancer with nanocaged doxorubicin prevents drug resistance and circumvents cardiotoxicity. *Oncotarget* **8**, 8383–8396 (2017).

Appendix

Most of the results presented in this elaborate have converged into a paper that is under submission. Moreover, in 2019 I attended the First EACR Conference of Nanotechnology in Cancer in Cambridge, where I shared this work in a poster.

During the Ph. D. period I took part to a project concerning the evaluation of a Zinc-doped iron oxide nanoparticle, studying in particular its properties as effective T_2 contrast agent:

Das, P. *et al.* Colloidal polymer-coated Zn-doped iron oxide nanoparticles with high relaxivity and specific absorption rate for efficient magnetic resonance imaging and magnetic hyperthermia. *J. Colloid Interface Sci.* 579, 186–194 (2020).